UC Riverside
UC Riverside Electronic Theses and Dissertations

Title

Envisioning the Invisible: Controlled Exciton Binding and Dissociation in a Tunable Type-I to Type-II TMD Heterojunction

Permalink
https://escholarship.org/uc/item/8vn1w4x7

Author

Kistner-Morris, Jedediah Joseph

Publication Date
2023

Peer reviewed|Thesis/dissertation

eScholarship.org
Powered by the California Digital Library
University of California

UNIVERSITY OF CALIFORNIA
RIVERSIDE

Envisioning the Invisible: Controlled Exciton Binding and Dissociation in a Tunable Type-I to Type-II TMD Heterojunction

A Dissertation in partial satisfaction
of the requirements for the degree of

Doctor of Philosophy

in

Physics

by

Jedediah Jospeh Kistner-Morris

December 2023

Dissertation Committee:
Dr. Nathaniel Gabor, Chairperson
Dr. Vivek Aji
Dr. Yongtao Cui

Copyright by
Jedediah Joseph Kistner-Morris
2023

The Dissertation of Jedediah Joseph Kistner-Morris is approved:

____

____

____

Committee Chairperson

University of California, Riverside

Acknowledgements

Science lives in conversation, and conversation requires people. The people I've met and the conversations I've had through my graduate career have foundationally shaped my identity as a scientist and as a person. We like to credit significant achievements to single people, but in reality every success is the culmination of a great network of thinkers and actors, none independent of the other.

I would first like to thank my advisor, Dr. Nathaniel Gabor. His passion for science, zeal for the unexplored, and eagerness to apply knowledge in new and exciting ways is inspirational. He has supported my scientific pursuits regardless of how outrageous they may seem. He has a unique ability to see to the heart of a measurement and draw out conclusions that many would miss. More than anything else I am immensely grateful to have worked with him during my time as a graduate student. Getting a PhD is a practice in failure, learning to succeed. Nathan made what is often a time of hardship and strife into one of joyous explorations.

I would like to thank my labmates, who were instrumental in my learning. Trevor Arp, Fatemeh Barati, Max Grossnickle, and Dennis Pleskott all served as mentors in their own rite. Jacky Wan provided an endless source of conversation, support, and a wealth of knowledge. Farima Farahmand, David Mayes, Esat Kilinc, and Zachary Miller were a delightful source of friendship and banter.

I would like to thank Ao Shi and Erfu Liu from Dr. Joshua Lui's lab. Device fabrication is one of the most difficult and emotionally taxing parts of condensed matter

research. Without their contribution of high quality samples my work would not have made it this far.

I would like to thank my fellow graduate students and all the friends I made along the way. It is bittersweet to have so many first hellos and so many goodbyes, hoping they won't be the last. The community I've found at UCR is supportive, creative, absurd, and brilliant.

Finally, I would like to thank my family. They formed the foundation for my curiosity and scientific drive. From the beginning they have supported me wholly and filled me with love.

To my late grandfather, Dr. Ottmar Kistner.

To my friends and family, who have fundamentally shaped who I am.

And to any future grad students, for whom this work is written.

ABSTRACT OF THE DISSERTATION

Envisioning the Invisible:
Controlled Exciton Binding and Dissociation in a Tunable Type-I to Type-II TMD Heterojunction

by

Jedediah Joseph Kistner-Morris

Doctor of Philosophy, Graduate Program in Physics
University of California, Riverside, December 2023
Dr. Nathaniel Gabor, Chairperson

We exhibit interlayer exciton mediated electron trapping via in situ band engineering in a two-dimensional semiconductor. The band alignment of vertically stacked $MoSe_2/WS_2$ heterobilayers is tuned between type-I and type-II by application of an out-of-plane electric field through the heterojunction. Precision tuning of the energy band alignment allows selective control over the formation and dissociation of interlayer excitons, which trap electrons at the atomic interface. The band alignment and excitonic energies are mapped via photoluminescence and dark transport measurements, exciton injection into the heterobilayer is determined via reflectance contrast, and charge carrier interactions are derived from photocurrent. These four measurements are then stitched together yielding a complete model of band alignment control and electron trapping. Using this model we are able to directly measure the binding energy of the interlayer exciton. These results provide a key contribution for next generation tunable quantum devices and controllable exotic interaction-based phenomena.

Table of Contents

Chapter 1 Control Through Many Perspectives **1**

1.1 The novelty of control: mutable band alignment and a tunable electron trap 1
1.2 The need for multiple perspectives 2

Chapter 2 Excitons in an Energy Landscape **5**

2.1 The power of small dimensions 5
2.2 The interaction of light and matter 7
2.3 Excitons and their flavors 8
2.4 Band alignments in semiconductor heterojunctions 10
2.5 Energy landscape of $MoSe_2/WS_2$ heterobilayers 11

Chapter 3 Electrical Control of the Heterojunction Interface **13**

3.1 Introduction 13
3.2 Voltage and field in heterojunction devices 13
3.3 Tuning the free carrier density 16
3.4 Tuning interlayer fields with V_{sd} and V_{bg}-V_{tg} 21
3.5 Electric field calculation for V_{bg}-V_{tg} 21
3.6 Electric field calculation for V_{sd} 23

Chapter 4 Nanofabrication of $MoSe_2/WS_2$ Heterobilayer Devices **26**

4.1 The ideal device 26
4.2 Substrate preparation 28
4.3 Writing Electrical Contacts via Electron Beam Lithography 29
4.4 Crystal exfoliation 30
4.5 Flake characterization 31
4.6 Lensed transfer 32
4.7 Microscope images of devices 33

Chapter 5 Imaging Techniques **35**

5.1 Imaging the energy topography and electron behaviors 35
5.2 Photoluminescence 36
5.3 Reflectance Contrast 37
5.4 Dark transport 37
5.5 Pulsed Photocurrent Microscopy 38

Chapter 6 Instrumentation **40**

6.1 Instrumentation 40
6.2 Photoluminescence and Reflectance Contrast 40
6.3 Dark Transport 42
6.4 Pulsed Photocurrent Microscopy 43
6.5 Parts list 47

Chapter 7 Photoluminescence and Reflectance Contrast 48
7.1 Mapping energetic absorption and emission 48
7.2 Doping and electric field dependent photoluminescence 48
7.3 Doping and electric field dependent Reflection 51
Chapter 8 Dark Transport and Photocurrent 54
8.1 Mapping single electron behavior and electron-hole interactions 54
8.2 Dark Transport 55
8.3 Dark I-V_g: electron-doped to charge-neutral crossover 55
8.4 Dark I-V_{sd}: junction rectification 57
8.5 Scanning Photocurrent Microscopy 58
8.6 Spatial photocurrent as a function of V_{sd} and V_g 60
8.7 $MoSe_2/WS_2$ junction photocurrent as a function of V_{sd} and V_g 62
8.8 I_{pc}-Power: Sublinear power behavior 64
8.9 Pulsed photoexcitation dynamics 66
8.10 Mapping relative decay rates 68
Chapter 9 Envisioning the Invisible 69
9.1 Building a complete understanding 69
9.2 Intrinsic band alignment and excitonic energies 70
9.3 Tunable band alignment and IX formation in an off twist device 72
9.4 Binding energy and dissociation estimation via I_{pc} 76
9.5 0 twist V_{bg}-V_{tg} control: exciton-polaron trapping 76
9.6 Spatial imaging of the electron trap 81
References 82
Appendix A Additional Datasets 87
A.1 V_{sd}<0 Photocurrent 87
A.2 I_{pc}-V_{sd} characteristics in device 4 88
A.3 PL of an off-twist device 88
A.4 Doping and electric field dependent photoluminescence response of device 3 89
Appendix B Electric Field Extraction from the Diode Fit 91
Appendix C A Puzzling Perspective 93

List of Figures

Chapter 1 Control Through Many Perspectives **1**

Figure 1.1 | Farima Farahmand, photographed with ultraviolet, visual, and infrared light 3

Chapter 2 Excitons in an Energy Landscape **5**

Figure 2.1 | Energy structure of WS_2 6
Figure 2.2 | Photoexcitation between parabolic bands 7
Figure 2.3 | Inter/intra layer and momentum direct/indirect excitons 10

Chapter 3 Electrical Control of the Heterojunction Interface **13**

Figure 3.1 | Schematic of a generic $MoSe_2/WS_2$ heterostructure with wiring diagram 14
Figure 3.2 | Effects of control voltages on band alignment and chemical potential...15
Figure 3.3 | Simple device schematic and equivalent circuit 17
Figure 3.4 | Charge carriers as a function of gate voltage determined by geometric capacitance and modified with quantum capacitance 19
Figure 3.5 schematic of a dual gated device with electric and displacement fields...22
Figure 3.6 | Energy band schematic describing the rectifying action of an ideal diode 24

Chapter 4 Nanofabrication of $MoSe_2/WS_2$ Heterobilayer Devices **26**

Figure 4.1 | Fabrication flow chart 28
Figure 4.2 | Photoluminescence response of monolayer $MoSe_2$ and WS_2 31
Figure 4.3 | Optical PL microscopy 32
Figure 4.4 | Diagram of a lensed stamp 33
Figure 4.5 | Microscope images of device 1, 2, and 4 34

Chapter 6 Instrumentation **40**

Figure 6.1| Optics schematic for photoluminescence and reflectance........................ 42
Figure 6.2 | Optics and signal schematic for photocurrent and dark transport........... 44
Figure 6.3 | Ray optic diagram from XY galvos to sample 45

Chapter 7 Photoluminescence and Reflectance Contrast **48**

Figure 7.1 | Field and doping dependent photoluminescence of $MoSe_2/WS_2$ heterobilayers at 4K 49
Figure 7.2 | Doping and electric field dependent reflectance contrast maps and their second-order derivates 52

Chapter 8 Dark Transport and Photocurrent **54**

Figure 8.1 Dark transport in a $MoSe_2/WS_2$ heterobilayer 55
Figure 8.2 | Tuning between charge neutral and electron doped regimes with V_g 56
Figure 8.3 | PN junction behavior and current rectification 57
Figure 8.4 Scanning photocurrent microscopy and optical images of devices 2 and 4 59

Figure 8.5 | Photocurrent images of device 2 at room temperature with varying V_{sd} and V_g 61
Figure 8.6 | Photocurrent response of $MoSe_2/WS_2$ heterobilayers....63
Figure 8.7 | I vs I_{pc} as a function of V_g and V_{sd} 64
Figure 8.8 | I_{pc}-Power behavior 65
Figure 8.9 | Charge carrier dynamics in a pulsed system....67
Figure 8.10 | Photocurrent and the relative rate of decay....68

Chapter 9 Envisioning the Invisible 69

Figure 9.1 | Band alignment and exciton binding energies in $MoSe_2/WS_2$....71
Figure 9.2 | Multi-measurement stitch of $MoSe_2/WS_2$ dynamics in devices 1 and 2.73
Figure 9.3 | Model for type-I to type-II alignment control and exciton binding vs. dissociation....75
Figure 9.4 | Multi-measurement stitch of $MoSe_2/WS_2$ dynamics in device 4....78
Figure 9.5 | Photoluminescence and photocurrent in device 4....80
Figure 9.6 | Model for type-I to type-II alignment control and exciton-polaron binding....80
Figure 9.7 | Envisioning a V_{sd} tuned electron trap....81
Figure 9.8 | Envisioning a gate tuned electron trap....81

References....82
Appendix A Additional Datasets....87

Figure A1 | Reverse bias photocurrent in device 2....87
Figure A2 | Photocurrent response of device 4 at room temperature....88
Figure A3 | Doping and electric field dependent photoluminescence response of an off-twist device....89
Figure A4 | Doping and electric field dependent photoluminescence map of device 90

Appendix B Electric Field Extraction from the Diode Fit....91

Figure B1 | Interlayer voltage extraction from dark transport in device 2....92

Appendix C A Puzzling Perspective....93

Figure C1 | Unit circle....93

List of Tables

Chapter 3 Electrical Control of the Heterojunction Interface....................................13

Table 3.1 | Effects of control voltages on electrostatic potential and fields.................15

Chapter 4 Nanofabrication of $MoSe_2/WS_2$ Heterobilayer Devices..............................26

Table 4.1 | Table of devices and performed measurements..34

Chapter 5 Imaging Techniques 35

Table 5.1 | Optoelectronic measurements 36

Chapter 6 Instrumentation 40

Table 6.1 | Common misalignments and their effects on image quality 46
Table 6.2 | Instrumentation Parts Lists for Photoluminescence & Reflectance 47
Table 6.3 | Instrumentation Parts Lists for Dark Transport and Photocurrent..............47

Chapter 1
Control Through Many Perspectives

1.1 The novelty of control: mutable band alignment and a tunable electron trap

Excitons, the bound state of an electron and hole, are one of the fundamental building blocks for a vast landscape of modern physics. Their behavior has been well studied across dimensions from bulk semiconductors[1] to zero dimensional quantum dots[2]. In two-dimensional semiconductors exciton interactions have led to a suite of exotic phenomena such as exciton-polarons[3], bi-excitons[4], correlated states[5,6], and excitonic liquids[7]. Foundational to these phenomena is the electronic energy landscape.

Energy band engineering is pivotal to the development of modern technologies. The functionality of everything from LED's to solar cells devices depends on the energy landscape of its material. A single device that can be band engineered in situ is therefore highly desirable. Conventionally, a heterojunction of two semiconductors exhibits either a type-I, type-II, or type-III alignment. Band alignment can be altered between devices of the same material system by altering strain[8,9], interlayer distance[8,9], and chemical doping[10–13]. There is experimental evidence for electric field tunable band alignment[14], and type-I to type-II switching has been proposed based on first principle simulations[8,15]. Despite this, a single device that can actively be switched between type-I and type-II alignments has never been experimentally observed.

In this work I will show how we tune $MoSe_2/WS_2$ heterobilayer junctions between a type-I and type-II band alignment, and how that in turn leads to the emergence of a tunable electron trap mediated by the formation of interlayer excitons across the

interface. This is approached through multiple imaging techniques that when combined will allow precision control and visualization of an exciton trap. Heterobilayer devices can be fabricated with a variety of electromagnetic controls and geometric designs. Charge trapping in these systems can thereby be finely tuned and would be of significant utility towards both new exotic phenomena and technological applications, such as quantum well tunable Bose-Einstein condensates and quantum computing.

This dissertation is laid out across nine chapters. In this chapter I will discuss the experimental philosophy that guides our approach to research. Chapters two and three cover the physics background necessary for this work including characteristics of transition metal dichalcogenide (TMD) heterobilayers and methods for electrical control of nanoscale devices. Chapter four describes the nanofabrication process for the devices used in this research, while chapters five and six discuss measurement theory and instrumentation. Chapters seven and eight present the primary results of our four imaging techniques and chapter nine combines the results together into a single unified model and discusses its implications. Appendix A presents additional datasets, B discusses electric field calculations, and C is a gift for those who endeavor to read this work in part or entirety.

1.2 The need for multiple perspectives

Scientists are perhaps the most aware of how little we perceive of the world. Consider our eyes, which contain four types of photoreceptors that can respond to light in an approximate range from 380 to 700nm. Compare that to the emission spectrum of the

sun, which bathes the earth with photons of wavelength all the way from 250 to 2500nm. Modern digital cameras are modified to reproduce this limited perception. Complimentary Metal-Oxide-Semiconductor (CMOS) sensors are coupled to a glass plate that reflects all but the visible wavelengths of light. This makes the camera capture images that reflect the behavior of our visual system, but also trims away a vast amount of beauty and information. This glass plate can be removed, and in doing so we open our perception, gaining knowledge we couldn't have accessed before.

Figure 1.1 | Farima Farahmand, photographed with ultraviolet, visual, and infrared light Ultraviolet photography is exceptionally sharp and reveals invisible freckles, skin features, patterns on plants, and atmospheric haze. Infrared photography is soft and ethereal, plants reflect strongly in IR giving them a blue or white sheen. Infrared astrophotography captures additional cosmic structures.

As a species we have evolved to fit into our niche environment, and as scientists we develop ways of thinking and skills that are perfected to our induvial fields. Specialization is not inherently bad, but collaboration, the combining of disparate views, is where new knowledge is born. String theory attempts to unify QFT and general relativity, neuroscience is inseparably linked to gut health, and CRISPR-Cas9 gene editing was developed from the immune system of bacteria. We can only begin to approach a full understanding when we combine data from varied sources and unify ways of thinking from many places.

This theme has proliferated through my own work. Melding physics and biology into a statistical understanding of photosynthesis[16,17]. Melding physics, data science, and sociology to map the spread of internet memes through social networks[18]. And here, combining imaging techniques all fundamental to condensed matter physics but rarely seen in one place to demonstrate a so-far unique electron trap. Condensed matter labs often specialize either in surface measurements, photo emission and absorption measurements, or transport and photocurrent measurements. The research that produced this dissertation is the result of collaboration between Dr. Gabor's optoelectronics lab, and Dr. Liu's photonics lab. We combine data from four different measurement techniques, taking what was at first a curious photocurrent feature and elevating it into evidence for band alignment engineering in an active device. This contributes to a foundation for next-generation devices and exotic states of matter that have yet to be manifested.

Chapter 2

Excitons in an Energy Landscape

2.1 The power of small dimensions

The restriction of dimensions and symmetry are two of the most profound forces in the universe. These two ideas form the basis for the entirety of condensed matter physics. As electrons are spatially restricted, whether by reducing dimensionality or breaking spatial symmetry via a latticed potential, they no longer ascribe to classical forms of behavior. A classical particle can exist in any state on a continuous spectrum of energy. The states available to a confined particle are limited and their energies become quantized. In periodic materials this leads to the emergence of energy bands[19].

The band structure, or dispersion relation, describes the energy of electronic states in a material as a function of momentum[i]. Semiconductors exhibit a band of forbidden energies for which no states exist. This band gap separates the valence band (VB) from the conduction band (CB). We define the highest energy state in the valence band as the valence band maximum (VBM) and the lowest energy state in the conduction band as the conduction band minimum (CBM). In real materials the band structure is extremely complex, however in 2D semiconductors we can estimate the dispersion relation near the band edges to be parabolic in nature,

$$E(k) = \frac{h^2 k^2}{2m} \tag{1}$$

[i] In this work momentum is generally taken to mean crystal momentum.

The electrochemical potential, μ, describes the energy required to add an electron to the system. At reasonable temperatures it is nearly identical to the fermi energy, E_F, which describes the highest occupied energy state in the system at zero temperature. The occupation of states at finite temperature is described by the Fermi-Dirac distribution

$$f(\varepsilon) = \frac{1}{e^{\varepsilon-\mu/k_B T}+1} \tag{2}$$

μ defines the energy at which the distribution equals ½. As temperature goes to zero the distribution becomes a step function. Many of the measurements in this study are performed at room temperature where $K_B T$=25.7meV.

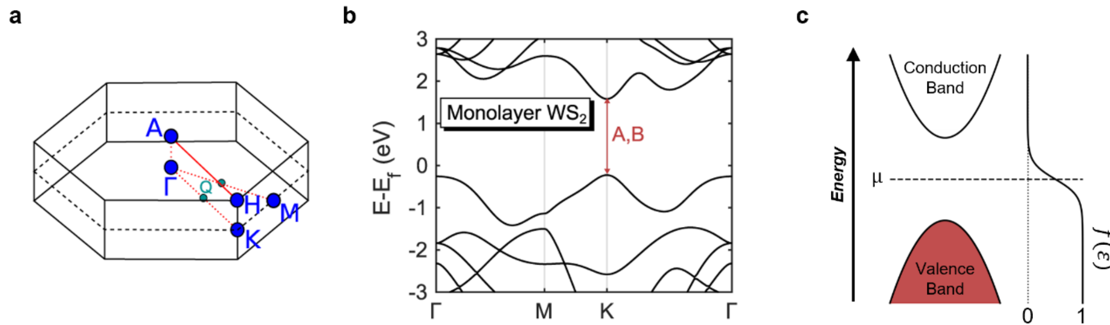

Figure 2.1 | Energy structure of WS_2 a, First Brillouin zone of a honeycomb lattice. High symmetry points in reciprocal space are marked. **b,** Calculated band structure of WS_2. All MX_2 (M=Mo, W; X=S, Se) TMDs share a similar structure. The smallest energy gap between the valence and conduction bands is marked. **c,** Schematic of the energy bands and Fermi-Dirac distribution describing charge carrier occupation. Near the band edges the conduction and valence bands are approximately parabolic. Here the valence band is completely filled and the conduction band is empty. Panels a and b are modified from (A. Chaves 2020)[20].

The occupation of free charges in the system and the band structure determine the energy of the electrochemical potential. If μ is inside the band gap and the temperature is low the valence band will be entirely filled with electrons and the conduction band

entirely empty (Figure 2.1c). This system is said to be charge neutral. The lack of free carriers means charge cannot flow.

2.2 The interaction of light and matter

The conduction band minimum and valence band maximum in monolayer TMDs exist at the same point in momentum space. As a result, these materials interact very strongly with light. An incident photon with requisite energy can excite an electron from the valence band into the conduction band[21]. The promotion of the electron across the energy gap leaves behind an empty state, or hole. While quasiparticulate in nature the hole has very real effects.

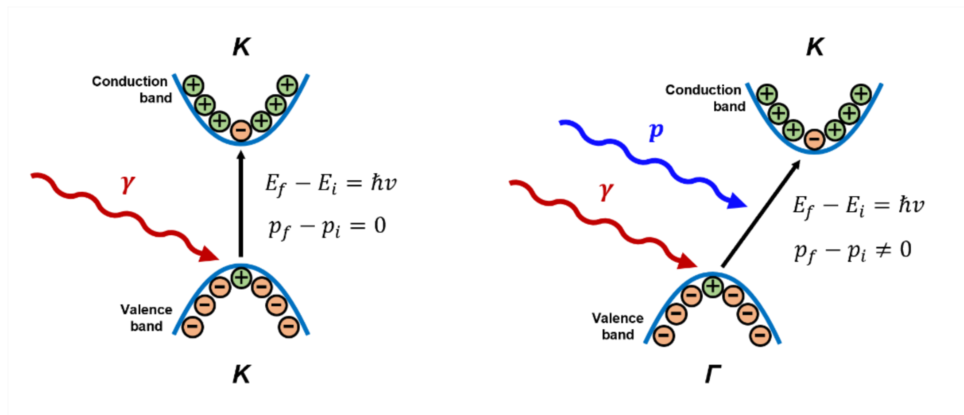

Figure 2.2 | Photoexcitation between parabolic bands a, An electron in a state at the VBM is promoted to one at the CBM by absorbing a photon. The photon energy must equal the energy difference between the states and the two states must have the same momentum. **b,** Photoexcitation between states with different momentum is possible but is a multipart process involving both photon absorption and phonon scattering. These complex transitions occur at a much lower rate. The distribution of electrons and holes in this schematic is only for visualization and does not represent a real density of states.

All of the mathematics describing the motion of electrons can be equivalently performed with holes. Electrons have fundamental charge $e=-1.602 \times 10^{-19}$C while holes have charge $-e=1.602 \times 10^{-19}$C. Electrons move to lower energy states by falling to the bottom of the conduction band while holes move to the lower energy states by falling up to the top of the valence band. Perhaps most fascinating of all is that electron-hole pairs can bind together into excitons, a quasiparticle that very much resembles the electron and proton of a hydrogen atom.

2.3 Excitons and their flavors

Commonly generated from a photoexcited electron-hole pair the exciton can appear in several forms. Electrons may be promoted across the band gap and then fall into an excitonic state, alternatively the exciton may be generated directly from a photoexcitation. In the latter case exciton generation is greatly enhanced when the stimulating light is resonant with the exciton energy. When formed the excitonic bound state has a lower energy than simply the difference between the state energies of the electron and hole. This binding energy represents the energy required to break the exciton back into electron and hole. Excitons decay either radiatively by recombining and emitting a photon (a bright exciton) or via phonon relaxation (a dark exciton).

Energy and momentum must be conserved for all transitions. Particle interaction rates are largely determined by wavefunction overlap. Therefore, the characteristics of excitons are largely determined by the physical location of the electron and hole as well as their location in energy-momentum space. Excitons are classified as either ***inter*** or

intra layer as well as momentum ***direct*** or momentum ***indirect***[22]. Figure 2.3 showcases these different forms.

Intralayer excitons exist in a single material. The electron and hole wavefunctions have a large spatial overlap and so a high rate of interaction, or large oscillator strength. This increased interaction rate means that intralayer excitons are often short lived as they easily recombine. All two-dimensional TMDs with elemental form MX_2 (M=Mo, W; X=S, Se) have conduction band maximum and valence band minimum at the same momentum[20]. The critical K point in momentum space represents the lowest energy step across the band gap in these materials. Excitons will naturally relax towards this energy minimum if possible. As a result, intralayer excitons in these materials tend to be momentum ***direct*** and can radiatively recombine emitting a photon. In 2D materials the intralayer electron and hole exist same material plane and so have a dipole moment that is in plane with the semiconductor.

Interlayer excitons consist of electrons and holes in different materials. The excitonic wavefunction exists across the interface of the two materials. These excitons have a lower oscillator strength often resulting in surprisingly long lifetimes[23]. The long lifetimes of interlayer excitons are enhanced by the fact that they are often momentum ***indirect*** and so cannot decay radiatively. The valance band maxima and conduction band minima still occur at the K points of their respective materials, but these points are only aligned in reciprocal space if the semiconductors themselves are stacked such that the relative twist between their crystal lattice is 0° or 60°. The dipole moment of the interlayer exciton is out of plane relative to the heterobilayer.

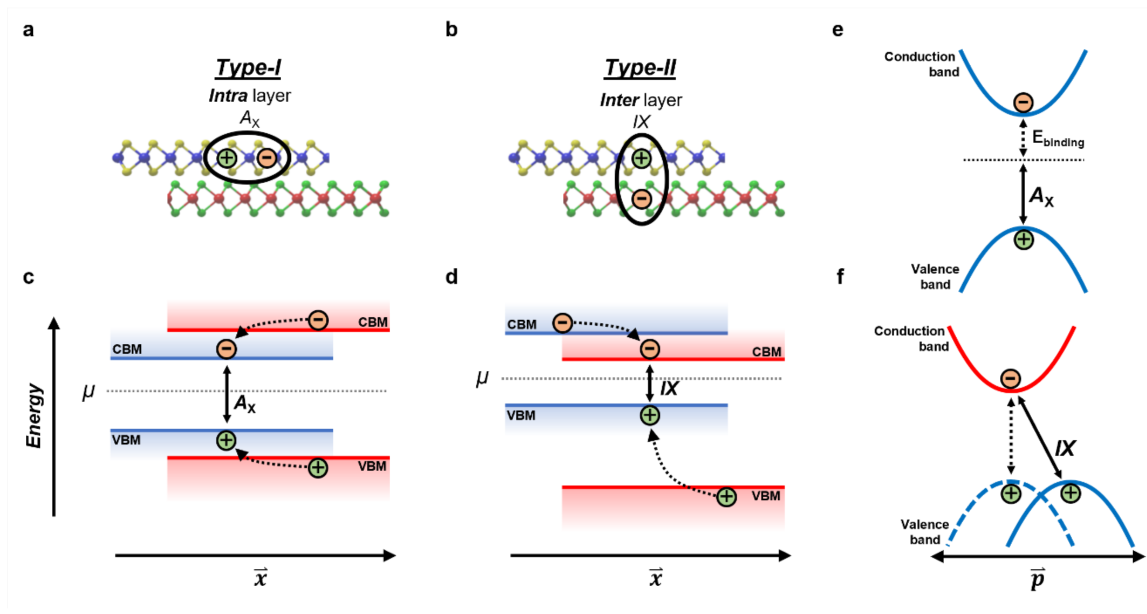

Figure 2.3 | Inter/intra layer and momentum direct/indirect excitons a, An electron and hole bound into a intralayer exciton. **b,** An electron and hole bound into an interlayer exciton. **c,** Type-I band alignment, the heterojunction conduction band minimum and valence band maximum belong to the same material. Electrons and holes funnel from the blue valence and conduction bands to the red valance and conduction bands. The lowest energy state in this system is an electron-hole pair in the blue material. An intralayer exciton is visualized. **d,** Type-II band alignment, the CMB and VBM belong to different materials. When the chemical potential is in the gap an electron in red and hole in blue form the lowest energy electron-hole pair. An interlayer exciton is visualized. **e,** A momentum direct intralayer exciton, the binding energy is also shown. **f,** A momentum indirect interlayer exciton (dashed line) vs its momentum direct counterpart (solid line). The momentum direct exciton can radiatively recombine but its counterpart cannot. Binding energy is not shown for the interlayer exciton.

2.4 Band alignments in semiconductor heterojunctions

The type of exciton that a material supports depends primarily on its electron energy landscape, or more broadly its band alignment[23]. Band alignment in semiconductor heterojunctions falls into one of three categories: type-I (straddled), type-II (staggered), and type-III (broken).

In the type-I, or straddled, band alignment, the band gap of one material resides completely within the band gap of the other, *i.e.,* both the conduction band minimum and valence band maximum belong to the same material (Figure2.3c). Charge carriers naturally move to lower energies therefore electrons and holes funnel into the same material. This supports the formation of momentum direct intralayer excitons in TMD heterojunctions. The short excitonic lifetime and high oscillator strength is ideal for applications in light emitting devices[24,25].

In the type-II, or staggered, band alignment the CBM of the heterostructure resides in one material and the VBM resides in the other (Figure2.3d). Such staggered alignment causes the photoexcited electrons and holes to relax to different materials. This facilitates electron-hole separation and hence favors applications in photodiodes[26,27] and photocatalysis[28]. Interlayer excitons are more likely to form in a type-II band alignment. It is important to note that is it possible for intralayer excitons to be energetically favorable in a type-II alignment if the binding energies have a large enough difference.

The type-III, or broken, band alignment will not be discussed in detail here. This energy alignment exhibits novel charge tunneling and is useful for applications in photodetectors and unique diodes[29,30].

2.5 Energy landscape of $MoSe_2/WS_2$ heterobilayers

The intrinsic band alignment of $MoSe_2/WS_2$ makes it an ideal candidate for in situ band engineering and control. These heterobilayers exhibit nearly degenerate conduction bands and so toe the line between type-I and type-II alignments[31]. Moderate application

of electric field could therefore have significant impact on the electron energy minima and maxima. In this work we will experimentally determine the alignment to be type-I.

Chapter 3
Electrical Control of the Heterojunction Interface

3.1 Introduction

Control of the energy landscape is achieved by careful control of the electrostatic potentials and fields through a heterojunction. Two primary tuning parameters are the electrostatic potential at the interface, V_T, tuning the density of free carriers, and the out-of-plane electric field, E, tuning the relative energy of the bands. It is beneficial to have control over the in-plane electric field, E_T, as well. Unfortunately, E_T depends on several often-hidden parameters such as device geometry, contact resistance, and the shape of the material layers themselves. We concede the ability to control ET with precision and settle for knowledge of its existence and direction.

In this chapter I discuss the ways we can tune these parameters by controlling the voltages applied to a heterojunction device. The effects of gate voltage on the free carrier density will be discussed. I also address the two ways we drive electric field through the device and calculations that convert control voltages into interlayer fields.

3.2 Voltage and field in heterojunction devices

Achieving a high level of control over the electrostatic potentials and fields through a heterojunction interface requires specific design consideration in device fabrication. Figure 3.1 shows a schematic of a generic device. A heterobilayer junction of $MoSe_2$ and WS_2 is sandwiched between protective hexagonal boron nitride (hBN). On either side of

the hBN lies a thin layer of metallic graphite. Each material layer (excluding the hBN) should be electrically contacted such that applied voltages can be independently controlled. V_{tg} and V_{bg} describe the voltages applied to the top and bottom graphene, V_g the voltage applied to the Si backgate, and V_{sd} the voltage applied across the heterojunction.

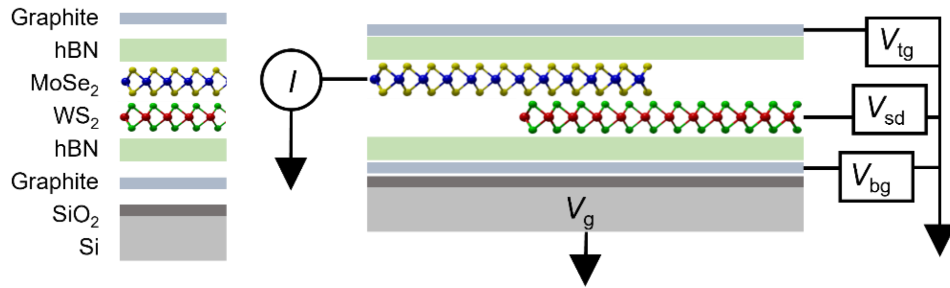

Figure 3.1 | Schematic of a generic $MoSe_2/WS_2$ heterostructure with wiring diagram. A generic device consists of a vertical stack of thin materials. Metallic grapahite is used to generate electric field through the device while hBN insulates the heterobilayer. V_{bg} and V_{tg} control the voltages applied to the bottom and top graphite gates respectively. V_g controls the voltage applied to the conductive Si within the Si/SiO_2. V_{sd} is applied across the TMD junction. The figure shows V_{sd} applied to WS_2 while current is collected from $MoSe_2$, this orientation can be reversed in situ.

The influence of tuning each voltage on E, E_T, and V_T are described below and in figure 3.2. The sum of the top and bottom gates, $V_{bg}+V_{tg}$, and V_g influence the chemical potential, μ. Application of V_{sd} across a heterojunction generates both an in-plane and out-of-plane electric field as the voltage drops spatially through the device. Out-of-plane electric field can also be independently generated by tuning the difference between top and bottom gates, V_{bg}-V_{tg}. The in-plane-field tilts the bands, and the out-of-plane field shifts their relative alignment. Electron energy states vary with electrostatic potential

$$U = q\phi \tag{3}$$

Energy bands are comprised of these states and so the junction alignment will shift with constant field according to

$$\vec{E} = -\nabla\phi \tag{4}$$

$$\Delta U = eEd \tag{5}$$

Where e is the fundamental electron charge and d is the separation between layers.

Table 3.1 | Effects of control voltages on electrostatic potential and fields

V_{sd}	*Primarily tunes* E & E_T, *and influences* V
V_g	*Primarily tunes* V_T *and influences* E
$V_{bg}+V_{tg}$	*Tunes* V_T
$V_{bg}-V_{tg}$	*Tunes* E[ii]*

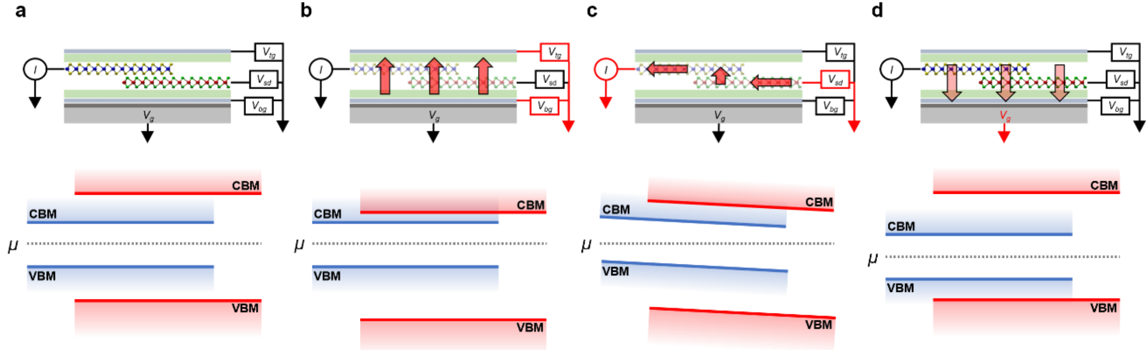

Figure 3.2 | Effects of control voltages on band alignment and chemical potential

a, The intrinsic $MoSe_2/WS_2$ band alignment. The type-II alignment is greatly exaggerated. **b,** Tuning $V_{bg}>V_{tg}$. An electric field is applied vertically through the heterojunction. The WS_2 experiences a higher electric potential than $MoSe_2$ and so its bands shift down. **c,** Positive V_{sd} is applied to WS_2 and $MoSe_2$ is grounded. This generates a voltage drop both through and across the layers. WS_2 bands are shifted down relative to $MoSe_2$. Additionally, the bands spatially tilt. **d,** Applying negative V_g lowers μ but also applies a small vertical field through the layers.

[ii] $V_{bg}+V_{tg}$ will also tune V_T (And $V_{bg}-V_{tg}$ E) if the encapsulating hBN thicknesses are not exactly equivalent.

A reasonable question one might ask looking at these dependencies is why use V_{sd} and V_g rather than V_{tg} and V_{bg}? Practically, it is much more difficult to fabricate devices with graphite top and bottom gates that do not contain accidental ground loops or other issues that interfere with transport based measurements. Functionally, several types of transport measurements require applying a transverse electric field. Though its dependance is complex it is an extremely useful control to have. Alternatively, the only redeeming factor of V_g over tuning the sum of gates, $V_{bg}+V_{tg}$, is that it can be easily implemented in any device fabricated onto a Si/SiO_2 substrate.

3.3 Tuning the free carrier density

The occupancy of free electrons is of fundamental importance to photonic and transport properties. The ability to control the free carrier density is therefore of great utility. The number of electrons in a system depends on the electrochemical potential, μ, and the energy band structure. μ is determined by the electrostatic potential at the interface. Increasing V_g or $V_{bg}+V_{tg}$ draws electrons into the system, decreasing these voltages does the opposite.

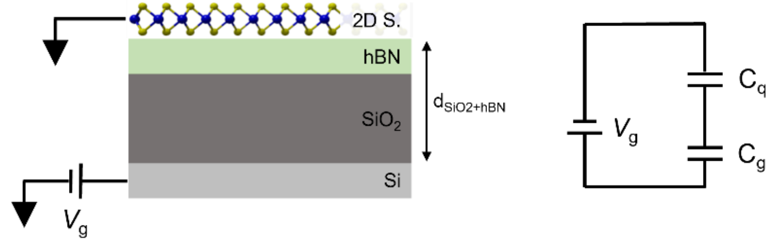

Figure 3.3 | Simple device schematic and equivalent circuit. A two-dimensional semiconductor (2D S.) separated from conductive silicon backgate by insulating SiO_2 and hBN. V_g voltage is applied to Si, the 2D S. is connected to ground. The equivalent circuit is described by two capacitors in series with the geometric capacitance (which depends on layer separation and the dielectric constant that fills the gap) and the quantum capacitance (which is determined by the density of states in the 2D S.).

Deriving the capacitance of a vertical device yields the relationship between charge density and V_g. Capacitance generally describes the charge a system gains per applied voltage,

$$C = \frac{Q}{V} = \frac{Ne}{V} \tag{6}$$

Consider a vertical device of a two-dimensional semiconductor (2D S.) separated a distance, d, from metallic Si by insulating layers of SiO_2 and hBN (shown in figure 3.3). The geometric capacitance between the Si and the semiconductor is given by:

$$C_g = \frac{\epsilon A}{d} \tag{7}$$

Where ϵ is the combined dielectric of SiO_2 and hBN. Applying a positive voltage to the Si moves from Si to the 2D S. An electron in metallic Si does not necessarily have the same energy as an electron in the semiconductor, which has limited states. Therefore, the voltage required to transfer an electron from Si to the semiconductor is not wholly described by C_g. Additional energy is required to move the electron up into the next available energy state in the 2D S. energy structure.

The true capacitance of the system is smaller, behaving as if there are two capacitors in series, C_g and C_q[32]. This quantum capacitance depends on the density of states of the 2D S. and changes as the density of free carriers is tuned. The total capacitance of the system is expressed as

$$\frac{1}{C} = \frac{1}{C_g} + \frac{1}{C_q} \tag{8}$$

Where the quantum capacitance scales with the density of states, $g(\varepsilon)$.

$$C_q = g(\varepsilon)e^2 \tag{9}$$

Combining (5) and (6) we get

$$C_{Total} = \frac{C_g C_q}{C_g + C_q} = \frac{Q}{V} = \frac{eN}{V_g} \tag{10}$$

and so

$$N(V_g) = \frac{V_g}{e}\frac{C_g C_q}{C_g + C_q} = \begin{cases} \frac{V_g}{e} C_g \; if \; g(\varepsilon) \gg 1 \\ \frac{V_g}{e} C_q \; if \; g(\varepsilon) \ll 1 \end{cases} \tag{11}$$

Knowledge of the density of states reveals how charge injection is tuned by V_g. If the chemical potential is in the band gap there are no states to occupy. $g(\varepsilon) \rightarrow 0$ and $C_g >> C_q$. The total capacitance is dominated by the vanishingly small quantum capacitance. Increasing the gate voltage does not change the number of carriers in the system as there is not enough energy to add a carrier to the conduction band. The electron density is "infinitely incompressible". When μ is inside either the conduction or valence bands the semiconductor has a large density of states and so $C_g << C_q$. The geometric capacitance is dominant and the system charges like a conventional parallel plate capacitor.

As the chemical potential passes into the conduction or valence bands C_g~C_q. Solving (11) explicitly requires the exact form of the density of states. For real materials g(ε) has nontrivial form and is calculated through theoretical simulation. Fortunately, we can approximate it near the band edge by treating the semiconductor as a two-dimensional electron gas with parabolic energy dispersion. This gives:

$$C_q = \frac{g_v m^* e^2}{\pi \hbar^2} \quad (12)$$

Where m^* is the effective mass and g_v the valley degeneracy. Treating C_q as a constant near the band edge allows us to approximate how the gate voltage tunes carrier injection into the system. The total capacitance and geometric capacitance of a hypothetical device are compared in figure 3.4.

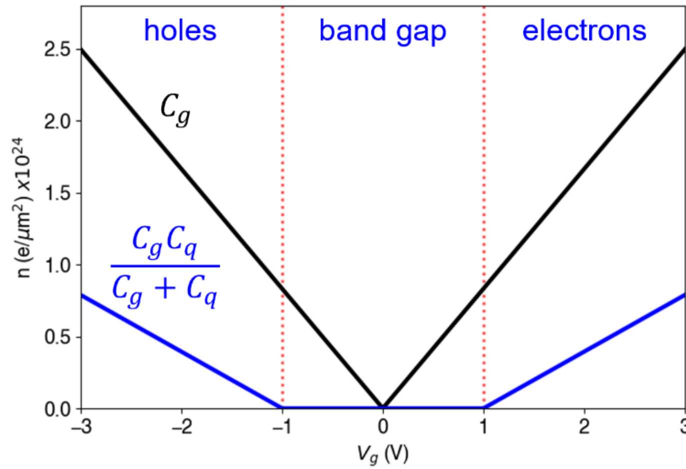

Figure 3.4 | Charge carriers as a function of gate voltage determined by geometric capacitance and modified with quantum capacitance. Black curve, number of free charges per square micron injected into a parallel plate capacitor separated by a distance of 315nm. Blue curve, number of free charges for a capacitor with the same geometry but one of the plates is a 2D semiconductor with $m_h^*=m_e^*= 0.01m_0$. This curve is only a valid approximation near the band edges.

The above analysis of device capacitance is common when analyzing the circuitry of gated heterojunction devices. Energy conservation provides a more intuitive alternative. To add an electron to the semiconductor energy is required to both move the electron into the material (relating to the geometric capacitance) and promote it to the next available state (increasing the electrochemical potential).

$$e\Delta V_g = e\Delta\phi + ed\Delta\mu \quad (13)$$

The total energy added to the system relates to the applied voltage, this energy is split between increasing the electric field between the layers and increasing the chemical potential in the semiconductor.

The above discussion applies to tuning the charge density with either V_g or $V_{bg}+V_{tg}$. The two control schemes function similarly, however, there are several key differences. When tuning the junction and maintaining a constant gated sum such that $V_{tg}=V_{bg}$ the entire area between the gates is at an equipotential, there is no electric field. Alternatively, the single gate produces a voltage gradient that extends normal to the surface. The semiconductor experiences a lower electrostatic potential that depends both on the dielectric and the distance from the gate. Furthermore, the single gate does generate an out-of-plane electric field through the semiconductor. In the case of two parallel metallic plates the second plate would completely screen the electric field. Because the semiconductor does not generate mirror charges at the same rate as the metal it does not completely screen the field. Some field is applied through the semiconductor shifting the

energy of the band structure. The screening effect changes with the density of states and is most pronounced when the chemical potential is in the band gap.

3.4 Tuning interlayer fields with V_{sd} and V_{bg}-V_{tg}

Control of the out-of-plane electric field is critical to tuning the band alignment in heterojunction devices. This can be accomplished by applying different voltages to the top and bottom gates or by applying a source-drain voltage across the junction. Control with V_{sd} generates both an out-of-plane and in-plane electric field through the heterojunction; control with V_{bg}-V_{tg} only tunes the out-of-plane field. Simultaneously utilizing V_{sd} and V_{bg}-V_{tg} provides a high level of control over E and E_T. The following two sections describe methods to calculate the out-of-plane electric field for control with V_{sd} and V_{bg}-V_{tg}.

3.5 Electric field calculation for V_{bg}-V_{tg}

Applying different voltages to the top and bottom gates ($\Delta V = V_{tg} - V_{bg}$) drives a potential gradient through the junction, generating an electric field. A schematic of the device geometry is shown in Figure X.

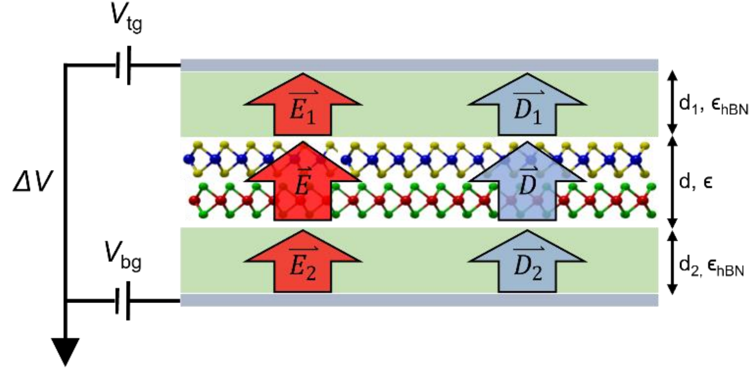

Figure 3.5 schematic of a dual gated device with electric and displacement fields

The semiconductor junction is sandwiched between two layers of hBN with thickness $d_{1,2}$ and dielectric constant ϵ_{hBN}. The voltage difference between the top and bottom gates constitutes the vertical field through the layers:

$$\Delta V = \int \vec{E} \cdot d\vec{l} \tag{14}$$

and so

$$\Delta V = d_1 E_1 + dE + d_2 E_2 \tag{15}$$

The displacement field through the device changes only where there is a free charge density,

$$\vec{D} = \epsilon \vec{E} \tag{16}$$

$$\nabla \cdot \vec{D} = \sigma \tag{17}$$

If the gates are tuned such that charge neutrality is maintained there are no free carriers in the junction and the displacement field is equivalent in each layer,

$$\epsilon_{BN} E_1 = \epsilon E = \epsilon_{BN} E_2 \tag{18}$$

Combining equation (15) and (18), we obtain

$$E = \frac{\Delta V}{\frac{\epsilon}{\varepsilon_{\text{BN}}}(d_1+d_2)+d} \quad (19)$$

We take d=1.2nm and $\epsilon=\epsilon_{MoSe2}=4.4$ for the heterobilayer; $d_{1,2}$=15nm and $\epsilon_{hBN}=3.4$ for the hexagon boron nitride. Plugging in these values yields

$$E = \frac{\Delta V}{40.02nm} \quad (20)$$

3.6 Electric field calculation for V_{sd}

Deriving the electric field generated from application of V_{sd} across a heterojuncion is more complicated than its gated counterpart. V_{sd} is applied to one layer of the junction relative to ground. The voltage drops both across the interface and through the materials generating both out-of-plane and in-plane field, E and E_T. It is difficult to calculate a value for E_T as this depends on many uncontrolled parameters such as contact resistance and flake geometry. We are usually resigned only to recognize its existence and sign. Alternatively, we can often calculate the generated out-of-plane field by calculating the voltage drop between the layers.

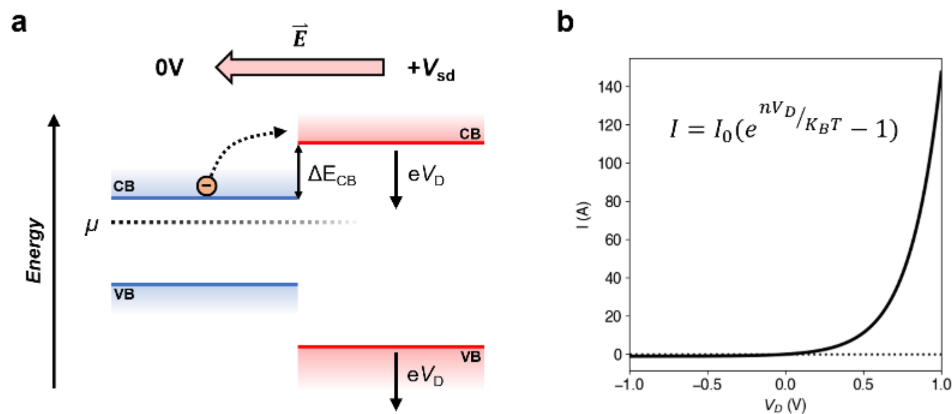

Figure 3.6 | Energy band schematic describing the rectifying action of an ideal diode **a,** Energy band schematic with a conduction band offset. The chemical potential is tuned such that electrons begin to populate the blue material but not the red. As positive voltage is applied to the red material its energy bands shift downward allowing electrons to move from left to right. There are no electrons in the red material to move from right to left. **b,** This mechanism is described by the diode equation.

Semiconductor heterobilayers with an energy difference between their conduction or valence bands form atomically thin pn junctions[33]. The energy band difference generates a stepped energy landscape that results in one directional current rectification. Figure 3.6 shows a hypothetical heterobilayer where the two materials have different conduction band energies. An electron in the red material will spontaneously move to the lower energy blue band, however electrons in the blue material cannot spontaneously jump to red. Electrons can be driven from blue to red by generating a red-to-blue pointing electric field, lowering the energy barrier between the conduction bands, ΔE_{CB}. If the chemical potential is tuned near the conduction band minimum electrons will occupy the CB of blue, but not of red. We can drive electrons from blue to red, but there are no charges in red to drive to blue. This mechanism is described by the diode equation

$$I(V_{SD}) = I_0(e^{enV_{sd}/k_BT} - 1) \tag{21}$$

Here n is the ideality factor. It effectively represents a lever arm between the applied external voltage, V_{sd}, and the actual voltage drop between the layers, V_D, that tunes the energy barrier at the interface, eV_D/k_BT. V_D contains the effects of V_{tg}, V_{bg}, and V_g. Importantly V_D does not contain any effects induced by contact resistance, device geometry, etc.

So long as the device is in a regime where (21) describes the charge carrier dynamics we can fit the transport curve, $I(V_{sd})$, and extract n. The electric field can then be calculated as

$$E = \frac{nV_{sd}}{d} \tag{22}$$

Where d is the metal ion to ion distance between the layers as this will constitute the bulk of the voltage drop. Precise details on the fitting procedure and algorithm for device 2 and 4 can be found in appendix B.

Chapter 4
Nanofabrication of $MoSe_2/WS_2$ Heterobilayer Devices

Fabricator's breakfast:
1 part cold brew coffee
1 part vodka
Cream and sugar to taste

4.1 The ideal device

The goal of fabrication is to make a heterojunction that can be carefully controlled and from which clear data can be measured. The ideal device contains a substantially large overlap, a clean interface free of major defects, independent electric contacts to each layer, and is fully encapsulated to protect it from the environment. Strong measurable interactions between layers demand an atomically sharp interface free of debris. Precision control of charge carrier behavior and band alignment requires careful control of the electric fields and potentials though the heterojunction. Photocurrent and dark transport measurements depend on a simple junction circuit with no ground loops or shorts. Robust reproducible results depend on samples that degrade slowly and so must be protected from oxidation, however this protection should not introduce physical stresses or charge doping in the device.

Combining all these elements in a single device is an extraordinary feat requiring skills that take years to master. It is no surprise that the greatest source of suffering for many condensed matter graduate students is that of device fabrication. The data presented in the main text of this dissertation come from three devices fabricated by Ao Shi and myself. The inclusion of top and bottom gates varies between devices however the

stacking order of graphite/hBN/$MoSe_2$/WS_2/hBN/graphite/SiO_2/Si is universally maintained.

The basis of the fabrication process begins with high quality, single layer semiconductor flakes, and a clean SiO_2/Si substrate to build the device on. A general fabrication process contains the following steps:

1. Si/SiO_2 chips are cut to an appropriate size and cleaned of oils and debris.
2. Gold contacts are written onto the Si/SiO_2 substrates.
3. Bulk crystal materials ($MoSe_2$, WS_2, hBN, Graphite) are exfoliated into thin flakes.
4. Flakes are selected and characterized via ramen spectroscopy and photoluminescence.
5. Select flakes are picked up and stacked via polycarbonate-based dry transfer.

This process is a combination of techniques developed and perfected by many other scientists. It has been specialized for the hBN/$MoSe_2$/WS_2/hBN geometry though alternative fabrication processes exist and new techniques are constantly being developed[34,35].

Every device maker develops their own style and techniques with time. This chapter is not designed to serve as an all-encompassing repository of fabrication techniques, this already exists. Rather it presents an overview of the process we use for our devices and shares the niche knowledge I have developed over years of arduous nanofabrication in the hopes that it aids future students.

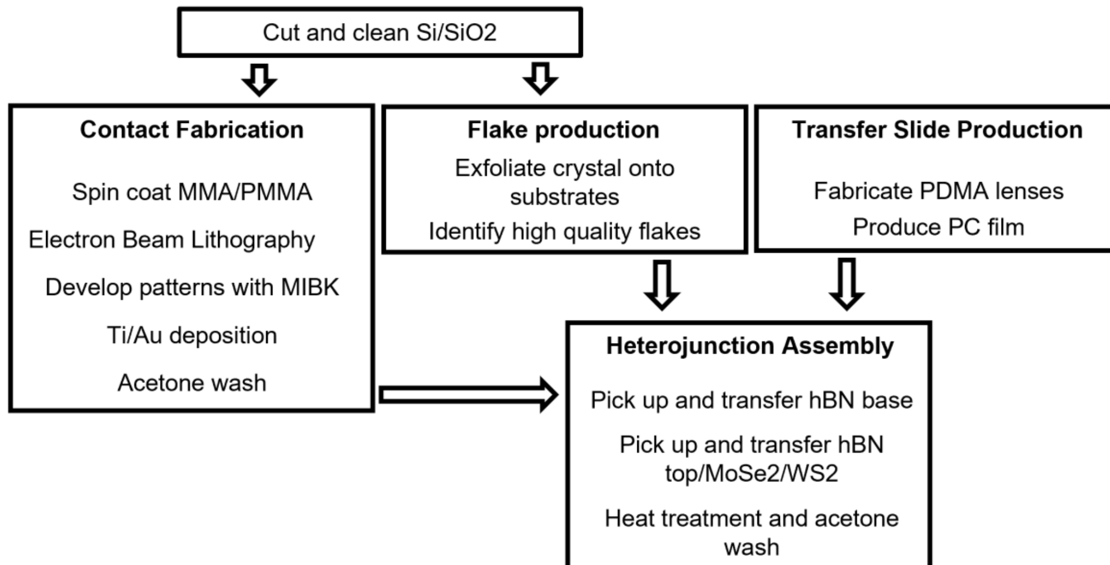

Figure 4.1 | Fabrication flow chart

4.2 Substrate preparation

Cleanliness is close to godliness only in that clean systems are simple and therefore easily understood in the same way we pretend that God is. The heterobilayer devices in this manuscript are built on Si/SiO_2 substrates. We start by using a diamond scribe to cut Si/SiO_2 wafers into 5-10mm square pieces. These squares are cleaned with acetone and then isopropyl alcohol. The substrates are farther washed with purified water if it is available. Each cleaning step acts to remove oils and debris along with residue from the previous solvent. It is sometimes beneficial to clean the surface of the substrates with plasma. This removes all organic residues from the surface of the SiO_2 and dramatically increases adhesion of thin films[36]. It is not always desirable as a perfectly

clean Si surface may bind so strongly to thin crystal flakes such that they cannot be removed without damage.

4.3 Writing Electrical Contacts via Electron Beam Lithography

Electron beam lithography and metal vapor deposition are the primary tools for electrically contacting heterobilayer devices. Contacts can be written before or after the heterobilayer is stacked onto the silicon substrate. The major advantage of prefabricating contacts is that it prevents accidental high energy electron-beam exposure of the heterobilayer. It is also a simpler fabrication process as there is only one lithography/deposition step and pre-fabricated contacts can be produced in bulk quantities. Post fabricating contacts has some increased risk of damaging the heterojunction however arbitrary geometries can be contacted.

The contact writing process starts with a clean Si/SiO_2 substrate. A layer of MMA copolymer is spin coated onto the surface at 4000rpm for 40s. The polymer is then cured on a hot plate at 180°C for 10 minutes. A second layer of PMMA EL 4 electron beam resist is spin coated and cured in the same manner. The pattern for the contacts is designed using the Nanometer Pattern Generation System (NPGS) which is then loaded onto a Leo XB1540 focused ion beam milling system with EBL capabilities. The MMA/PMMA coated flake is loaded into this system, and the pattern is exposed onto the surface. The pattern is developed using a 1:3 MIBK:IPA mix which dissolves the electron-beam exposed polymer. The developer is then rinsed off using IPA then purified water. Following this 4-10nm of Ti and 25-75nm of Au are deposited onto the substrates with an electron beam evaporator. The initial application of titanium acts as a binding

agent between the gold and the SiO_2 surface. Lastly the substrate is soaked and washed with acetone which removes the remaining polymer and unwanted Ti/Au, leaving behind only the desired contacts.

4.4 Crystal exfoliation

Bulk crystals are exfoliated into thin flakes using dry tape exfoliation[3]. A small flake of bulk crystal is placed on a strip of tape which is folded onto itself and pulled apart repeatedly. Each iteration of this cycle shears the crystal, producing increasingly thin flakes. These flakes are transferred from the tape to clean Si/SiO_2 substrates. The tape is carefully placed on the surface of the silicon which is then heated on a hot plate at 60-100°C for 1-10 minutes to soften the glue of the tape and increase flake adhesion to the SiO_2 surface. The tape is then slowly peeled off the silicon leaving behind a patch of crystal flakes with varying thickness. The tape residue may be cleaned off with a quick acetone wash. Plasma cleaning may be utilized at this step as well to great effect[37].

The number of fold-and-pull iterations, the speed at which the tape is pulled apart, the pressure applied to the tape when placed on the substrate, the temperature and time spent on the hot plate, and the technique with which the tape is removed from the silicon all influence the number and quality of the single layer flakes that can be harvested. No two graduate students will agree upon the ideal parameters to produce each crystal type, and may themselves fail to produce quality flakes with any regularity. As stated by Dr. Vivek Aji, “Condensed matter physicists are very superstitious.”

4.5 Flake characterization

Potential candidate flakes for heterojunction devices are identified by optical microscopy. Flake quality is then confirmed via Ramen spectroscopy and/or photoluminescence. Single layer $MoSe_2$ and WS_2 have momentum direct band gaps that strongly emit at energies of 1.6eV and 2.0eV respectively. They are easily identified by both the emission energy and a greatly enhanced photoluminescence intensity when compared to their multi-layer counterparts[38,39].

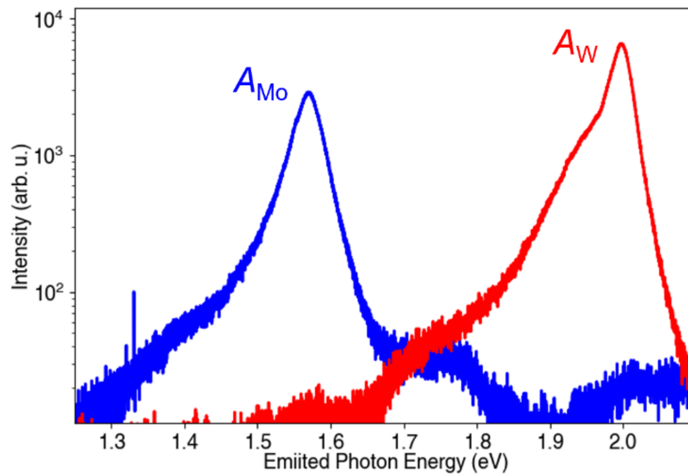

Figure 4.2 | Photoluminescence response of monolayer $MoSe_2$ and WS_2. The $MoSe_2$ B exciton is visible as a small peak at 1.75eV. The WS_2 trion emits at a lower energy than the WS_2 A exciton and is responsible for the asymmetric peak. Both these features are additional identifiers of single layer $MoSe_2$ and WS_2.

The photoluminescence of these materials is so powerful it can be directly observed under a microscope using a special set of filters. This dramatically speeds the identification of quality single layer flakes. Following the procedure described by Evgeny Alexeev and others[40]; we install a 550nm short pass filter into the polarizer and a 600nm

long pass filter into the analyzer of an optical bright field Nikon microscope. This illuminates flakes with only high energy light and allows the collection of low energy light near the PL emission peaks of these materials. Single layer materials have a large enough emission intensity that a several second camera exposure will capture the response. Exemplary flakes of WS_2 can even produce a response visible to the naked eye.

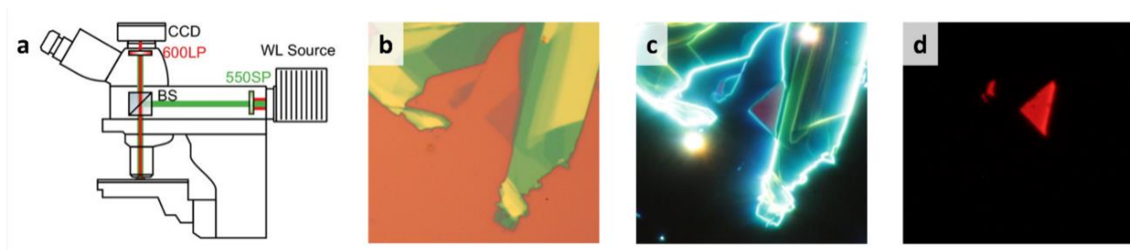

Figure 4.3 | Optical PL microscopy a, Diagram of the microscope with long and short pass filters (microscope schematic taken from Alexeev E. 2017) **b,** bright field image of a WS_2 flake. A triangle of single layer WS_2 is attached to the side of a multi-layer piece of bulk. **c,** dark field image of the same flake, the edges of the flake layers are illuminated. **d,** long exposure PL microscopy image of the same area. PL emission form the single layer WS2 is visible.

4.6 Lensed transfer

I utilize a dry transfer technique with lensed polydimethylsiloxane/polycarbonate (PDMS/PC) stamps. The dry transfer procedure has been well documented[34]. The only modification I make to it is the use of custom PDMS lenses[41]. The use of lensed PDMS reduces the contact area between the stamp and silicon substrate allowing for more precise pickups while limiting the chance of failure. The angled area of contact also serves to reduce trapped air bubbled between layers.

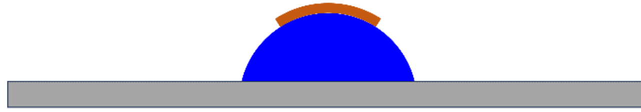

Figure 4.4 | Diagram of a lensed stamp (not to scale or proportional) showing glass slide (gray), PDMS (blue) and PC (orange).

Lenses are produced as follows. A batch of SYLGARD 184 Silicone Elastomer PDMS is mixed and allow it to sit for thirty minutes allowing most of the air bubbles to settle out. One to three drops of still liquid PDMS are placed onto the center of a clean microscope slide which is then immediately inverted and placed over a hot plate at 150°C to speed the cure time. To prepare for transfer a square piece of PC is placed at the apex of the lens. After the stacked heterojunction is deposited on the substrate I anneal completed samples on a hotplate at 100°C for several minutes to improve adhesion to the Si before removing the polymers with acetone.

4.7 Microscope images of devices

The data in this manuscript comes primarily from three devices. When referenced in this document the devices are listed as devices 1, 2, and 4 (to match the order in an upcoming publication). The original names are also given here for anyone unfortunate enough to find themselves sifting through old lab notes.

Table 4.1 | Table of devices and performed measurements

Device Name	***Mady By***	***Geometry***	***Twist***	***Measurement***
Dev 1 (Ao02)	Ao	Gr top/bottom gates and contacts	0º/60º	4K PL
Dev 2 (MW29)	Jed	Si backgate, Au contacts	Off twist	300K I_{pc}
Dev 3	Ao	Gr top/bottom gates and contacts	0º/60º	4K PL (Appendix A)
Dev 4 (Ao16)	Ao	Gr top/bottom gates and contacts	0º/60º	50K I_{pc} 4K PL
Dev 5	Ao	Gr top/bottom gates and contacts	Off twist	4K PL (Appendix A)

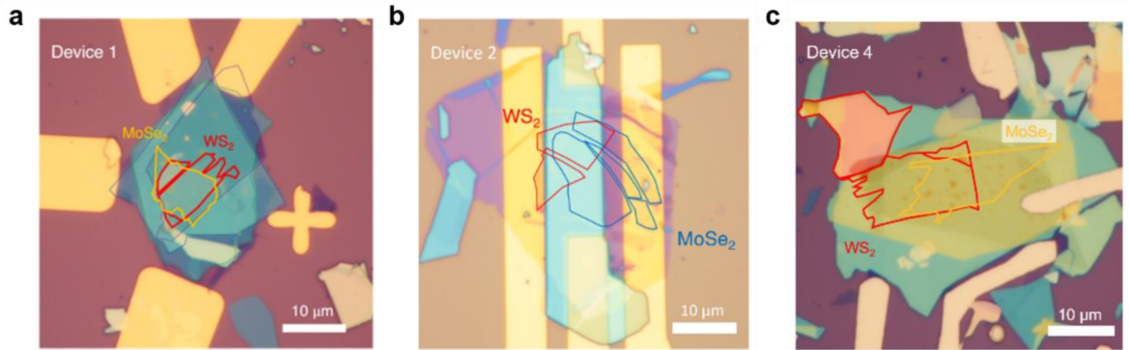

Figure 4.5 | Microscope images of device 1, 2, and 4

Chapter 5
Imaging Techniques

5.1 Imaging the energy topography and electron behaviors

Our goal is to image the energy landscape of $MoSe_2/WS_2$ and the behavior and interaction of electrons on that landscape. It is only when we meld an understanding of the mutable band alignment with the motion of carriers through the heterojunction that we can achieve full control of carrier interactions at the interface. Charge transport and emission measurements are directly influenced by band alignment and excitonic energies while photoexcited transport measurements inherently reflect electron interactions. Reflectance contrast measurements informs where photoexcitations occur in the system.

We therefore image the energy landscape with photoluminescence (PL) and dark transport measurements. Charge carrier behaviors are imaged with photocurrent microscopy and relative reflectance.

This chapter will introduce the four imaging techniques we utilize, what each technique tells us, and what factors each is sensitive to. A summary of the four techniques and their role in this work is provided below. Photoluminescence maps the excitonic energy landscape, dark transport maps the band alignment, reflectance constant maps photoexcitations, and photocurrent maps particle interactions. Due to the experimental similarities data for PL and reflectance contrast will be grouped together in chapter 7 as will dark transport and photocurrent in chapter 8. The data is brought together in chapter 9.

Table 5.1 | Optoelectronic measurements

	Used to image an energy landscape	*Used to probe the electron-hole behavior*
Photonic	**Photoluminescence** Green light is used to excite a population of high energy excitons. These decay and may radiatively recombine revealing the energies of the moment direct transitions.	**Reflectance Contrast** White light is projected onto the sample and the light that passes through is measured. This reveals absorbing transitions in the energy alignment.
Transport	**Dark Transport** Voltages are applied to one material and/or junction gates and current flow through the device is measured. Reveals single charge transport behavior.	**Pulsed Photocurrent Microscopy** Sample is illuminated with a pulsed laser and device current is measured. The behavior of photoexcited charges influences the current produced.

5.2 Photoluminescence

Photoluminescence measures radiative emission[42]. It is primarily sensitive to the lowest energy momentum direct transitions in a band structure. In a PL measurement a sample is illuminated with high energy light which excites a population of hot electrons above the conduction band and holes below the valence band. This population of excited carriers relaxes and cools, moving towards the conduction and valence band edges, dispersing energy through coulomb scattering and phonon interactions. These electron-hole pairs may form bound excitons.

An electron-hole pair can radiatively recombine and emit a photon at any time via band-to-band recombination. Similarly, an exciton may radiatively recombine. Both processes must conserve energy and momentum. Exciton recombination will emit a lower energy photon than band-to-band recombination as the binding energy reduces the total

energy of the exciton. The characteristic time for recombination is often much longer than that of relaxation, therefore emission energies strongly reflect energy band minima.

5.3 Reflectance Contrast

Where PL measures radiative emission, reflectance contrast measures radiative absorption. A sample is illuminated with broadband white light and the light reflected back is measured. Photoexcitation as a result of photon absorption can only occur across transitions for which momentum and energy are conserved. Transitions may either be band-to-band or excitonic, where excitonic transitions are more sharply defined in wavelength and at lower energies than band-to-band. Photoexcited transitions are strongly influenced by the oscillator strength. States with large spatial overlap of their wavefunctions will have higher absorption rates.

Reflectance contrast is always measured relative to a background. Reflectance spectra is measured both at the point of interest on the sample, R_{HJ}, and at some point far away from the heterojunction, R_{Si}. The absolute difference between these measurements is then normalized to the spectra from the substrate,

$$\frac{\Delta R}{R} = \frac{|R_{Si} - R_{HJ}|}{R_{Si}} \tag{23}$$

5.4 Dark transport

Dark transport measures the magnitude of charge carriers that move through a heterojunction interface. It is effectively a measure of resistance. One layer is connected

to a source voltage while the other is connected to an ammeter and ground, drain. The charge doping of the semiconductor is controlled through V_g or $V_{bg}+V_{tg}$. The flow of electrons through the heterojunction is primarily influenced by the relative band energies between the two semiconductors and the free carrier density.

5.5 Pulsed Photocurrent Microscopy

To measure photocurrent the heterojunction is probed with light and the current exiting the junction is collected. This is sensitive to many factors including radiative absorption, emission, and band alignment but is strongly influenced by charge carrier interactions within the heterojunction[43]. Ultrafast pulses of coherent light are pumped into the sample. The wavelength of light may be adjusted to be resonant with various radiative transitions in the energy landscape to photoexcite electrons into specific bands; it may be tuned to energies smaller than any photo-excitable transitions to study thermal properties; or it may be tuned to high energies to excite a large population of hot carriers. Once a population is photoexcited single carriers will move under the influence of the energy landscape (as one might measure with dark transport) but will also relax and cool to lower energy states (through the same mechanisms that influence photoluminescence). Photoexcited carriers can interact with each other in a variety of ways. Free electrons and holes may bind into excitons, excitons interact with other single carriers forming exciton-polarons[3] or driving auger processes[44], excitons can interact with other excitons forming biexcitons[4], correlated states[5,6], and even excitonic liquids[7]. These interactions influence the photocurrent in measurable ways.

Photocurrent measures the free charge carriers that exit a heterojunction as a result of a photonic pulse. The current produced by a single laser pulse depends on the time dependent population of charges, N(t), and the rate with which single charges escape the junction, α. N(t) contains information regarding carrier interactions, decay processes, and charge extraction. Measured photocurrent can be expressed as

$$I_{pc} = ef\alpha \int_0^\infty N(t)dt \tag{24}$$

where e is the fundamental electron charge and f is the excitation pulse frequency. This equation is valid so long as the time for the system to return to equilibrium is shorter than the time between pulses, otherwise a multi-pulse equation must be used[7]. Interpreting the photocurrent informs the behavior of N(t) which we can use to describe the complex behaviors within the junction.

Chapter 6
Instrumentation

6.1 Instrumentation

The instrumentation for this thesis is split between Dr. Gabor's lab, which performed the transport and photocurrent measurements, and Dr. Lui's lab, which performed the photoluminescence and reflectance measurements. Much of the instrumentation is shared between measurements. PL and reflectance are performed in the same cryostat and the two measurements share optics. Dark transport and photocurrent measurements are performed in a different cryostat with shared voltage controls and data acquisition.

The instrument schematics presented in this chapter show only the necessary optical elements for each measurement to be performed. When arranged on an optics table space and geometry restrictions will likely demand additional mirrors and lenses. Our experimental optics setups are living instrumentation. They are designed to encompass a large range of potential measurements and a real beam path may include delay stages, polarizers, additional neutral density filters, and more. An optics table is always in flux, a rigorous diagram with all elements may be obsolete within a month.

6.2 Photoluminescence and Reflectance Contrast

Photoluminescence and reflectance are performed in a closed-cycle cryostat held under high vacuum and mounted on an XY micrometer stage. The light source is a

532nm continuous wave laser which passes through a beamsplitter and is then focused onto the sample with an objective lens to a spot size of 1-2 μm. The same objective collects the emitted light and passes it back down the laser line to the beamsplitter which redirects into a spectrometer. The spectrometer is equipped with a CCD camera and coupled to a computer system that records the spectral intensity of the emitted light. V_{tg} and V_{bg} are controlled by two programmable voltage sources. Reflection contrast is performed using a nearly identical setup except the green laser is replaced by a white light source.

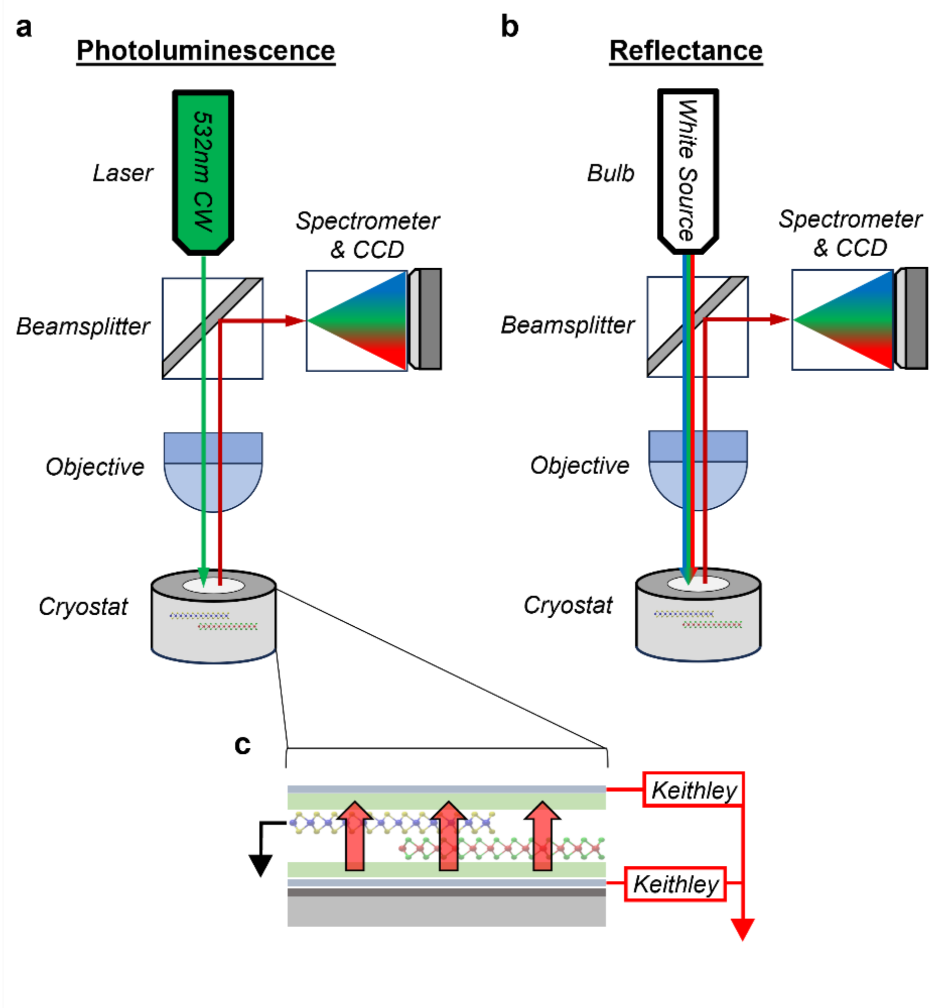

Figure 6.1| Optics schematic for photoluminescence and reflectance a, A 532nm continuous wave laser is focused onto the heterojunction held in a cryostat under high vacuum. The spectral intensity of the emitted light is measured with a spectrometer and CCD. **b**, The reflection setup is nearly identical except the green laser is replaced by a white light source. **c**, Voltages are applied to the graphite top and bottom gates via Keithley voltage sources that electrically feed into the cryostat.

6.3 Dark Transport

The experimental design for dark transport measurements also forms the basis for photocurrent. Devices are placed in a cryostat held under high vacuum using roughing and turbo pumps. A computer system equipped with Data AcQuisition cards (DAQs) is

used to apply V_{sd}, V_{tg}, V_{bg}, and V_g voltages. The DAQ cards are connected to the cryostat and sample by coaxial cables, interrupted by a switchbox that serves to isolate the device from the measurement system and allow rearranging cable connections without risking an electrical discharge to the heterojunction. Current leaving the device is converted to a voltage and boosted with an amplifier before being recorded by the same DAQ equipped computer system. We use the Multi-Parameter Dynamic Photoresponse Microscopy (MPDPM) hyperdaq software developed by Travor Arp to automate voltage control and data collection[45].

6.4 Pulsed Photocurrent Microscopy

Pulsed photocurrent microscopy is performed with the sample setup in a manner identical to dark transport. The excitation light path begins with a continuous wave 532nm laser that drives a Ti:Sapph laser cavity producing 150fs pulses at 75MHz. The cavity can be tuned to produce laser wavelengths from 700nm-850nm. The light passes through a pair of lenses to correct any aberrations from the laser cavity and produce a collimated beam. A chopper is placed at the focal point between the collimating pair to chop at the smallest beam waist. This chopper is coupled to a lock-in amplifier that will be used to isolate the photoexcited signal. A controllable and continuously variable neutral density filter is placed in the beampath so the laser power, or fluence, at the sample can be tuned.

Focusing the laser light into a scanning point on the sample uses a particular set of optics (elements 1-5 in figure 6.2) consisting of XY galvanometers (controllable mirrors)

a pair of collimating lenses, a beamsplitter, and the objective. With proper alignment a beam spot of ~2µm can be achieved. The intensity of the light passing through the beamsplitter is measured by an indium gallium arsenide (InGaAs) detector providing a relative measure of the laser fluence incident on the device. Light that reflects off the device moves back through the objective and beamsplitter where its intensity is measured by a second InGaAs detector. As the laser scans across the surface this produces an image of the spatial reflection intensity.

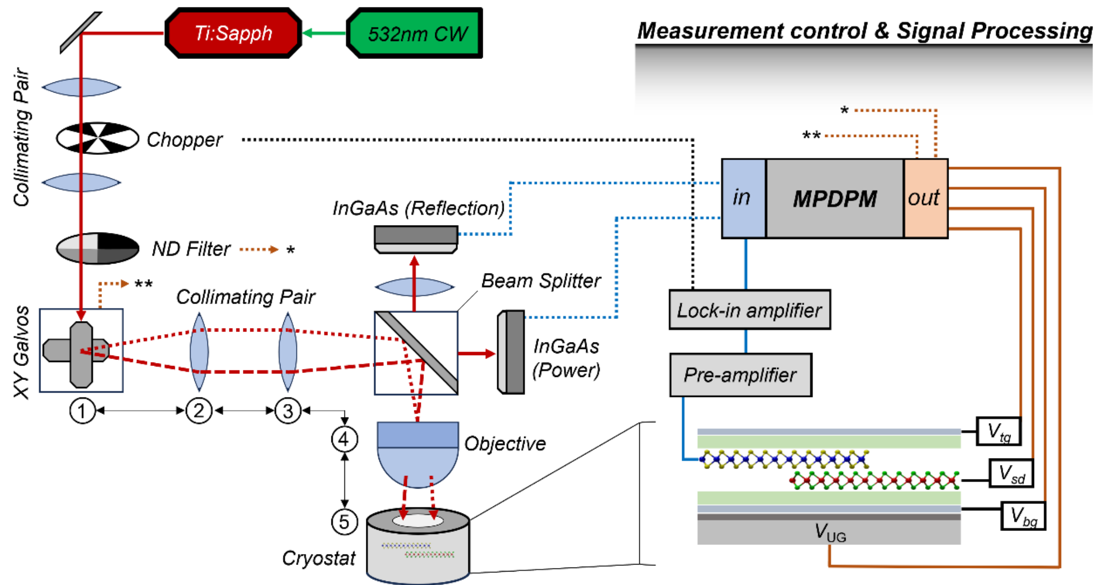

Figure 6.2 | Optics and signal schematic for photocurrent and dark transport. Solid red lines denote unchanging laser path. Dotted and dashed red lines show two example beam paths while the galvos are scanning the laser. Dotted blue and orange lines indicate input signals and control lines for accessories to the measurement such as power and reflection while solid blue and orange lines mark device voltage control and photocurrent signal acquisition.

The alignment of optics 1 through 5 is of particular importance. The XY galvos change the radial angle of the laser beam. Like focusing a point source, lens 2 must be

placed such that its distance from the galvo mirrors, 1, is equal to its focal length. 2 and 3 are collimating pairs and so their separation should equal the sum of their focal lengths. The moving angle out of the galvos should not change the beam position on the back of the objective therefore the distance from (3) to (4) should be equal to the focal length of lens 3. Finally, the objective is placed at its working distance from the device. This system is resilient to small deviations from alignment though they will degrade image quality. Understanding the ray optics that results in a focused beam spot on the device is important to diagnosing and understanding various alignment and image quality issues. Figure 6.3 draws two example beam paths with the galvos at different angles. Table 6.1 describes common misalignments in this system and their effects on image quality.

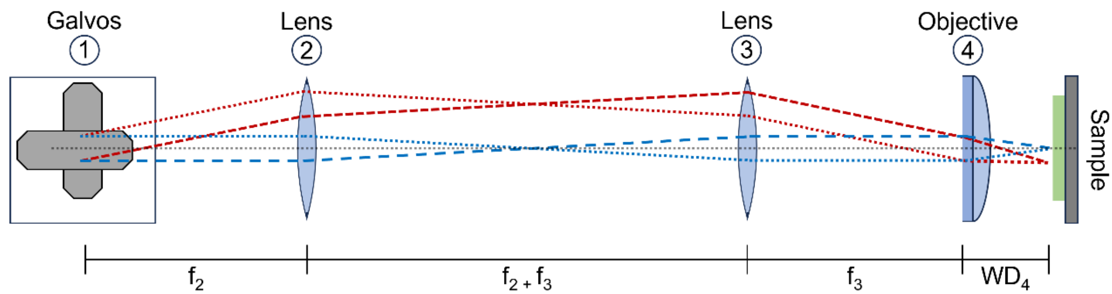

Figure 6.3 | Ray optic diagram from XY galvos to sample. Red and blue lines trace out the edges of two different beam paths, deflected from the galvos at different angles. For ease of viewing the beamsplitter has been removed from the diagram as it does not influence the optical spacing. For a real beam with physical lenses the beam will not compress to an infinitely small point. Note that the angle of light striking the device is not generally normal to the surface. This does not usually impact photocurrent measurements however it is important to note that the incident light wavefront is non-trivial.

Table 6.1 | Common misalignments and their effects on image quality

Alignment Problem	Effect
Objective not set to its WD	Low image resolution from larger spot size
Beam not collimated at objective	Low image resolution from larger spot size
Objective not at focal length of (3)	Image smearing and vignetting as laser translates off the objective
Distance 1-2 not equal to f_2	Image smearing and vignetting as laser translates off the objective

The photocurrent produced by the device is boosted by a pre-amplifier before being passed to a lock-in amplifier which is coupled to the chopper between the first collimating pairs. When tuned to the proper phase the lock-in isolates the signal so that only current produced by the laser photoexcitation is measured. This signal is then measured by the DAQ system in the same manner as dark transport.

6.5 Parts list

The exact parts used for each experimental setup are listed here. We measured photocurrent in two different cryostat systems, parts specific to each system are labelled in blue and red. The switchboard mentioned in section 5.3 is custom built in-house.

Table 6.2 | Instrumentation Parts Lists for Photoluminescence & Reflectance

Green laser	Laser Quantum Torus 532
White source	Thorlabs broadband light source SLS201L
Beamsplitter	Thorlabs 50:50 beamsplitter
Objective	40x Nikon S Plan Fluor
Cryostat	Closed cycle Montana Optical Cryostat
Spectrometer	Princeton Instruments HRS-500-MS
Voltage src.	Keithley K2400 source meter

Table 6.3 | Instrumentation Parts Lists for Dark Transport and Photocurrent

Green laser	Coherent Verdi
Ti:Sapph	Coherent Mira 900
Chopper	Thorlabs optical chopper system
ND filter	Thorlabs stepper motor rotation mount with round variable ND filter
XY galvos	Thorlabs galvanometer with power supply and servo drivers
Beamsplitter	Thorlabs 90:10 beamsplitter
InGaAs	Thorlabs free-space amplified photodetector
Objective	Edmund Optics 50x Objective
Cryostat	Lake Shore ST-100 series microscopy cryostat
Objective	Thorlabs gradient index of refraction (GRIN) lens
Cryostat	Custom Janis Research ST-3T-2 Optical Cryostat
Amplifier	DL instruments 1211 pre-amplifier
Lock-in	Stanford Research Systems Lock-in amplifier
DAQ	2x National Instruments DAQ card with 16 port breakout box

Chapter 7

Photoluminescence and Reflectance Contrast

7.1 Mapping energetic absorption and emission

In this chapter we will use photoluminescence and reflectance contrast to map the excitonic energy emission and absorption landscapes. PL reveals radiative transitions that occur at energy minima while reflectance informs the light sensitive transitions that promote electrons or generate excitons. Doping dependent PL shows clear transitions between a charge neutral intralayer exciton and positive or negatively charged exciton-polarons in $MoSe_2$. The field-dependent intralayer exciton emission begins to linearly stark shift when a critical electric field is generated through the interface. This implies formation of an interlayer exciton that can be switched on or off with field. Reflection contrast shows exciton promotion occurs only in $MoSe_2$ regardless of electric field.

7.2 Doping and electric field dependent photoluminescence

We first measure photoluminescence while tuning the top and bottom gate voltages such that $V_{bg}=V_{tg}$. This tunes the electrostatic potential at the interface, injecting charge carriers into the heterojunction while applying no electric field. The resulting emission map is shown in figure 7.1a

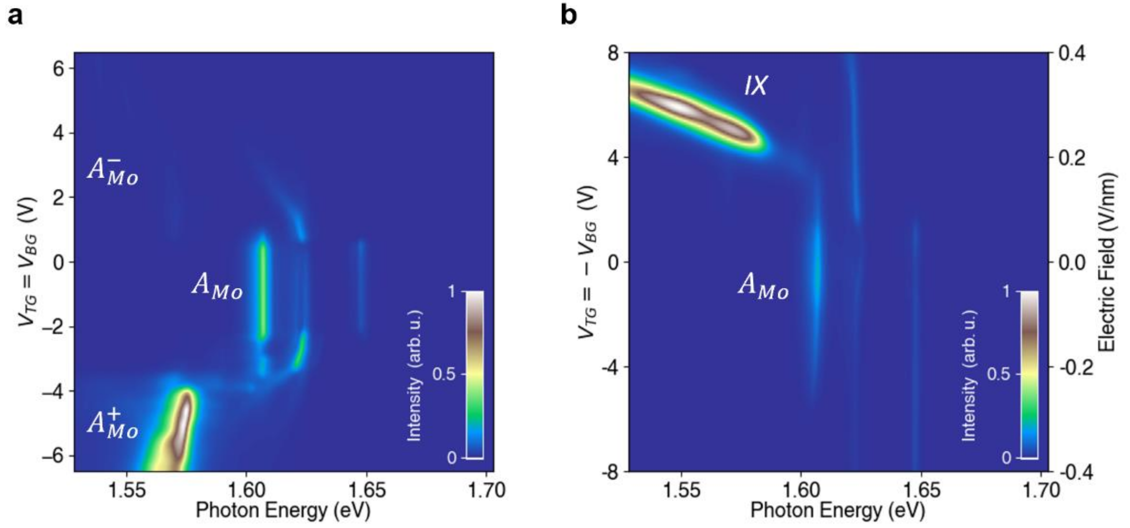

Figure 7.1 | Field and doping dependent photoluminescence of $MoSe_2/WS_2$ heterobilayers at 4K. a, Charge-density dependent PL emission map. Top and bottom gates are tuned at the same voltage (V_{bg}=V_{tg}) and photon emission energy is measured. **b,** Field-dependent PL emission map. Top and bottom gates are tuned at equal magnitude but opposite sign (V_{bg}=-V_{tg}).

When V_{bg}=V_{tg} is tuned between -3V and 1.5V the heterojunction exhibits a pronounced emission peak, A_{Mo}, at 1.61eV. This matches the reported energy of the A exciton in BN-encapsulated $MoSe_2$ monolayers[3,46,47]. When V_{bg}=V_{tg} is tuned outside these ranges electrons or holes are injected into the heterojunction and the A_{Mo} emission peak subsides. Two new peaks emerge ,A_{Mo}^{-} and A_{Mo}^{+}, ~30meV below the exciton on the electron and hole side respectively. This energy separation is close to the exciton-polaron binding energies in monolayer $MoSe_2$[3,46,47]. Additionally, the new PL peaks redshift with increasing charge density, this is consistent with the typical behavior of exciton-polarons. We therefore conclude that A_{Mo}, A_{Mo}^{-} and A_{Mo}^{+} arise from the intralayer exciton and exciton-polarons in the $MoSe_2$ monolayer. Also visisble are some weak lines on the higher energy side of A_{Mo}, but they are not reliably reproducible in other devices (see

appendix A for additional data sets). Possible effects may include the influence of moiré patterns, slight atomic reconstructions, and interface inhomogeneities in the heterostructure.

We repeat the previous experiment but now tune the gates such that V_{bg}=-V_{tg} while maintaining V_{bg}=V_{tg}=0 (Figure 7.1b). This generates an electric field through the heterojunction but does not change the charge carrier doping. The junction stacking order is bottom-gate/WS_2/$MoSe_2$/top-gate and so if V_{bg}>V_{tg} the electric field points from WS_2 to $MoSe_2$ (this direction is indicated by V_{tg}=-V_{bg}>0, ΔE>0). The conversion from V_{bg}=-V_{tg} to E was previously discussed in section 3.

When V_{tg}=-V_{bg} is small the A_{Mo} emission line is visible and its photon energy does not change with field. This indicates the excitonic dipole moment is orthogonal to the electric field direction and thus reinforces its intralayer nature. When the voltages are increased such that V_{tg}=-V_{bg}>3.4V (E = 0.16V/nm) the A_{Mo} line subsides and is replaced by a lower energy emission peak (*IX*) that redshifts linearly with increasing field at a rate of 44±11meV per 0.1V/nm. When E is increased past 0.23V/nm the emission intesnsity becomes exceptionally pronounced.

The linear shift of *IX* indicates it has an out-of-plane dipole moment such that its energy is tuned with field. The interlayer exciton consists of an electron and hole separated across the heterobilayer and therefore has a relatively simple expression for its dipole moment.

$$\vec{p}(\vec{r}) = \sum_{i=1}^{N} q_i(\vec{r_i} - \vec{r}) = ed \quad (25)$$

Where e is the fundamental electron charge and d is the distance between electron and hole. The energy of an electric dipole within a field is given by:

$$U = -\vec{p} \cdot \vec{E} \tag{26}$$

Combining (25) and (26) we calculate from the emission slope an electron hole separation of 0.4 ± 0.1nm. This is consistent with the width of the heterobilayer (W to Mo spacing of minimum ~0.6nm) and farther supports *IX* arises from the interlayer exciton.

The transition from $MoSe_2$ intralayer to $MoSe_2/WS_2$ interlayer exciton provides strong initial evidence for a type-I to type-II transition. There is yet a possibility that the binding energy of *IX* is so much larger (smaller) than that of A_{Mo} that the heterojunction remains in a type-I (type-II) band alignment with no transition. These results combined with the dark transport data in section 8 will solidify the nature of the transition to be that of a band alignment switch, which will be discussed in detail in section 9.

7.3 Doping and electric field dependent Reflection

We also investigate the absorption properties of the heterojunction via reflection contrast over the same V_{bg} and V_{tg} values. Figure 7.2a shows a reflection contrast map as a function of V_{tg}=V_{bg} and photon energy. The $MoSe_2$ intralayer exciton and exciton-polaron states are visible. The reflection lines are strongly localized indicating that the photoexcitation is generating excitons, rather than driving band-to-band transfer. In order to more clearly visualize these transitions we take the second derivative with respect to photon energy, shown in figure 7.2c-d.

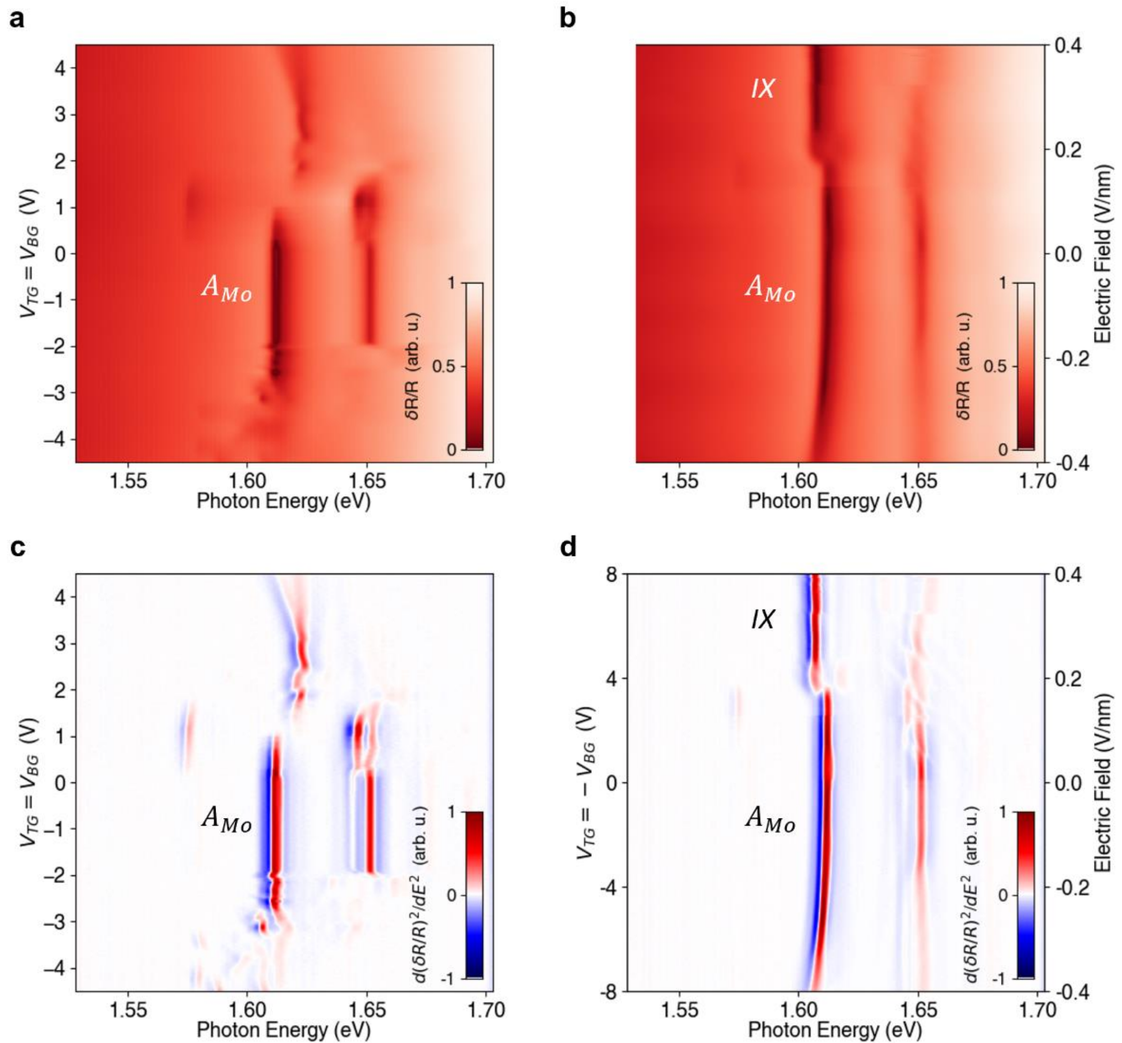

Figure 7.2 | Doping and electric field dependent reflectance contrast maps and their second-order derivates. a, doping depending reflectance contrast spectra. **b,** electric field dependent reflectance contrast spectra. **c-d,** second order derivatives with respect to photon energy.

Interestingly, the $MoSe_2$ intralayer exciton is observed at zero field however the stark shifting interlayer exciton, *IX*, is not present. This is reasonable as the interlayer exciton has much lower oscillator strength due to the spatial separation of electrons and

holes. Evidence for the *IX* state is not entirely absent, the absorption discontinuity around V_{bg}=-V_{tg}=4V indicates a mixing of the inter and intralayer states[48]. Most importantly this data signifies that even when formation of the interlayer exciton is energetically favorable, the intralayer exciton is photoexcited. The predominant emission of *IX* in PL indicates electron transfer from the conduction band of $MoSe_2$ to WS_2 to form the lower energy bound state.

Chapter 8
Dark Transport and Photocurrent

8.1 Mapping single electron behavior and electron-hole interactions

In this chapter we will use dark transport and scanning photocurrent microscopy to probe the behavior of single electrons and charge interactions. The movement of single electrons through a heterojunction is primarily determined by the relative alignment of its energy bands. The volume of photoexcited carriers that exit a heterojunctions depends on the types of charge carrier interactions that occur and are facilitated by the energy structure.

Dark transport reveals heterobilayer $MoSe_2/WS_2$ behaves as an atomically thin pn junction. Measurements reveal that charge neutrality to electron doping can be tuned with V_g while I-V_{sd} curves show dramatic rectification. Scanning photocurrent microscopy reveals an anomalous suppression in the photoexcited transport that originates at the junction overlap. Comparison with dark transport indicates this suppression occurs in the charge neutrality regime and may be the result of electron trapping at the interface. This behavior is farther investigated with power dependent photocurrent. A model of charge carrier dynamics is proposed to explain the I_{pc}-P behavior and reveals an increased ratio of multi-body decay processes to single-body decay processes. This indicates a switch from intralayer to interlayer excitons.

8.2 Dark Transport

Figure 8.1a shows a map of the current that moves through a $MoSe_2/WS_2$ junction as a function of V_{sd} and V_g at room temperature and in complete darkness. V_{sd} is applied to the WS_2 flake while current is collected from $MoSe_2$. Electrons must transit the interface to be measured. No current flows through the junction when V_{sd}<0V or V_g<-3V. As V_{sd} and V_g are increased, exponentially increasing charge flow is observed. The behavior becomes linear after an initial turn on but remains monotonic.

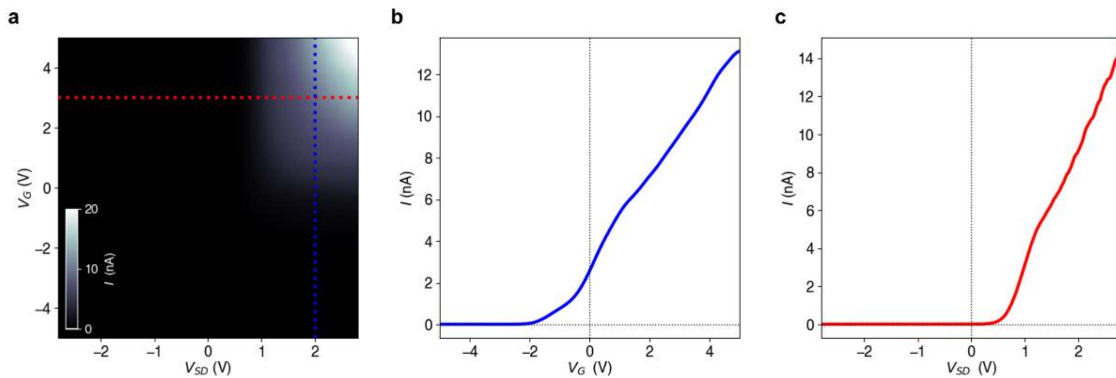

Figure 8.1 Dark transport in a $MoSe_2/WS_2$ heterobilayer a, Dark transport map as a function of V_{sd} and V_g. V_{sd} is applied to WS_2 while current is collected from $MoSe_2$. The measurement is performed at room temperature while the heterojunction is insulated from any stray light. **b,** I-V_g as V_{sd} = 2.0V. Currently increases monotonically but nonlinearly when V_g > -3.0V. **c,** I-V_{sd} at V_g=3.0V. Zero current flows when V_{sd} < 0V. An exponential turn on is observed between approximately 0V and 1.0V. Current linearly increases when V_{sd} > 1.0V.

8.3 Dark I-V_g: electron-doped to charge-neutral crossover

Controlling V_g allows us to tune the heterojunction between charge neutral and electron doped regimes. For current to flow there first must be free charge carriers in the system, i.e. there must be unoccupied states in the valence band or partial occupation of

the conduction band. Increasing V_g applied to the Si backgate draws electrons into the heterobilayer, raising the chemical potential μ. Figure 8.1b shows dark current as a function of V_g. The transition from zero current to monotonically increasing current around as V_g is tuned indicates a crossover from char e neutrality to n-type.

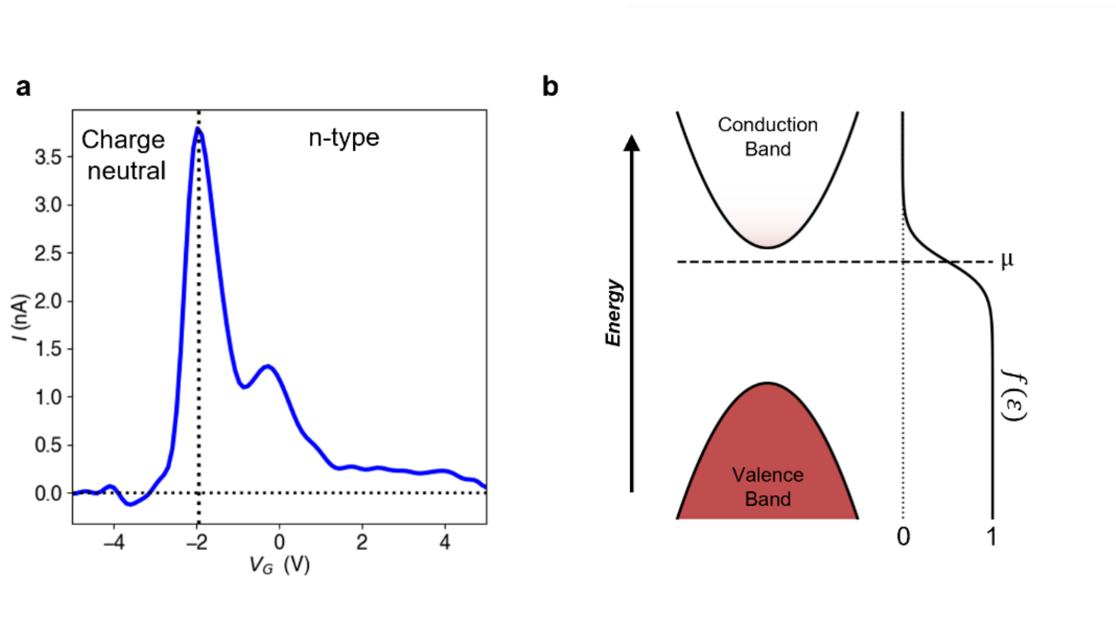

Figure 8.2 | Tuning between charge neutral and electron doped regimes with Vg a, d [log(I-V_g)]/dV_g at V_{sd} = 1.0V. The function peaks at V_g = 2.0V marking the transition between doping regimes. **b,** A schematic of the filling of the energy bands as described by the fermi-dirac distribution. At finite temperature the high end of the fermi-dirac distribution spreads out and electrons begin to populate the conduction band even though μ is inside the band gap.

The exact crossover voltage is calculated by taking the derivative of the natural log of the current with respect to V_g. This function peaks at the crossover voltage, V_g = -2.0V. Note that the crossover voltage does not correlate to the point where I-V_g first becomes nonzero. This measurement was performed at finite temperature, as a result

there is a distribution of electrons with energy greater than μ that occupy the conduction band while μ is in the gap.

8.4 Dark I-V_{sd}: junction rectification

Where the I-V_g dependence informs the charge doping of the junction, I-V_{sd} characteristics inform the energy landscape. I-V_{sd} curves in $MoSe_2/WS_2$ heterobilayers show strong rectification. Figure 8.1c shows current as a function of V_{sd} when V_g = 3.0V. When negative V_{sd} is applied to WS_2 no current flows, however positive V_{sd} drives monotonically increasing current with an exponential turn on.

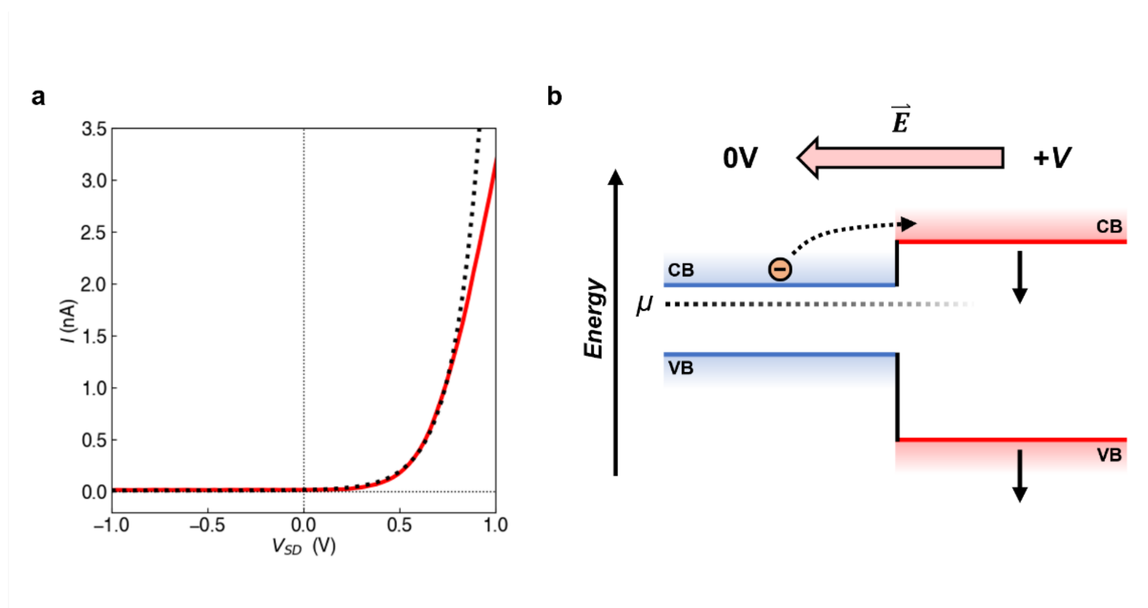

Figure 8.3 | PN junction behavior and current rectification. a, I-V_{sd} at V_g = 3.0V. The dashed black line is the best fit for the diode equation to the low V_{sd} data. **b,** Energy schematic of an atomic pn junction. Electrons populate the conduction band of $MoSe_2$ but not WS_2. The only way current can flow through the junction is if electrons transfer from $MoSe_2$ to WS_2 by lowering the energy threshold with an out of plane electric field.

This exponential behavior is well described by a pn junction and reveals an intrinsic type-I band alignment. The direction of current flow is critically influenced by the alignment of the energy bands. I-V_g characteristics indicate that current flow is mediated by free electrons in the conduction band. The sign of V_{sd} that drives increasing current informs which material these electrons originate from. Current exponentially increases when positive V_{sd} is applied to WS_2. This voltage application shifts the WS_2 energy bands down relative to $MoSe_2$. Electrons increasingly flow from the lower energy CB to the higher energy CB as the energy difference is reduced. Electrons cannot flow in reverse because the higher energy CB is not populated. This indicates the WS_2 conduction band has a higher energy than $MoSe_2$ when the junction is unbiased. The magnitude of their relative band gaps indicates the heterobilayer is intrinsically type-I.

8.5 Scanning Photocurrent Microscopy

Where dark transport reveals the behavior of single electrons as an integrated result of the entire heterojunction device scanning photocurrent microscopy probes local behavior of photoexcited carriers. Figure 8.4 shows photocurrent maps of devices 2 and 4 next to optical microscopy images.

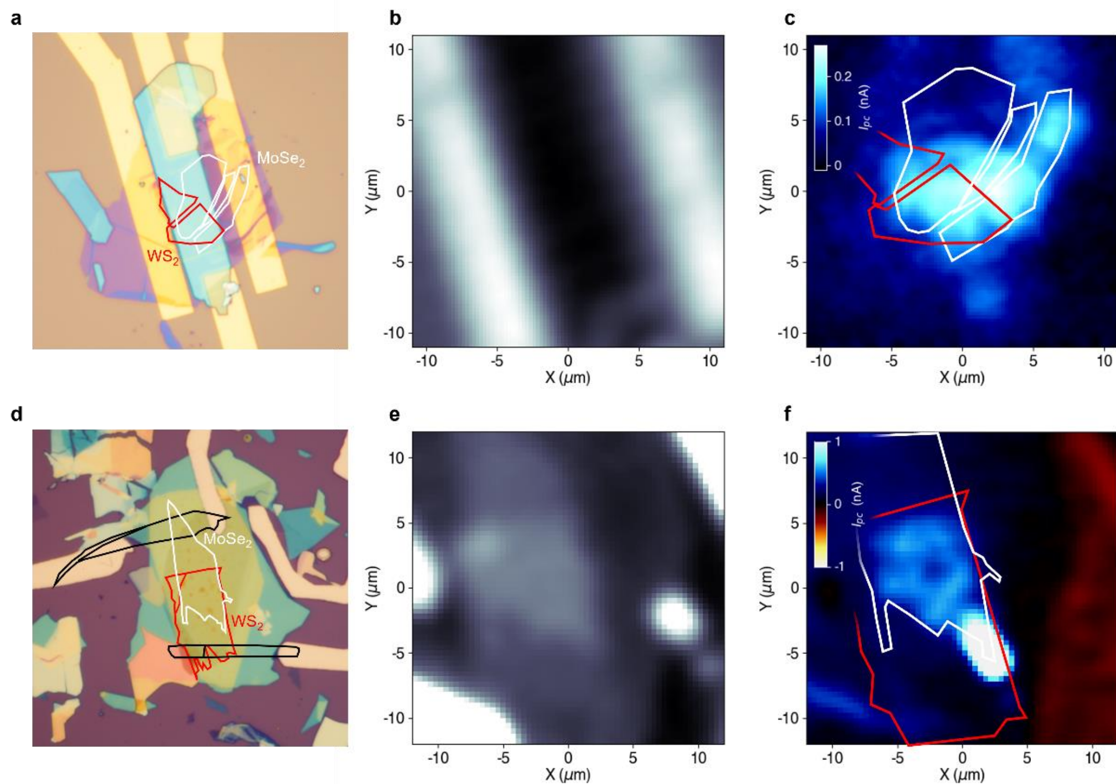

Figure 8.4 Scanning photocurrent microscopy and optical images of devices 2 and 4. a-c, Optical, reflection, and photocurrent images of device 2 **d-f,** Optical, reflection, and photocurrent images of device 4. $MoSe_2$ and WS_2 are outlined in white and red respectively.

Photocurrent mapping can be iterated over various parameters (V_{sd}, V_{tg}, V_{bg}, V_g, laser power, laser wavelength, temperature, pulse rate, etc.) to generate volumes of data that contain significant depth of information. The melding of dynamic control and data acquisitions comprises a consolidated technique, so named Multi-Parameter Dynamic Photo-Response Microscopy (MPDPM).

8.6 Spatial photocurrent as a function of V_{sd} and V_g

Spatial photocurrent mapping reveals an anomalous photocurrent suppression that originates from the $MoSe_2/WS_2$ overlap. Figure 8.5a shows a 50 by 27 grid of spatial photocurrent maps taken with an excitation wavelength of 830nm (1.5eV). Spatial "hypercubes" of this sort contain an immense volume of data, but to access it we must reduce the dimensionality of the dataset. Figure 8.5b shows six of these spatial photocurrent maps, repeated with increasing V_{sd}. The $MoSe_2$ and WS_2 layers are outlined in blue and red. Both the $MoSe_2$ and overlap produce photocurrent that grows and evolves with increasing V_{sd}. WS_2 produces no photocurrent as the excitation energy is considerably less than the WS_2 energy gap.

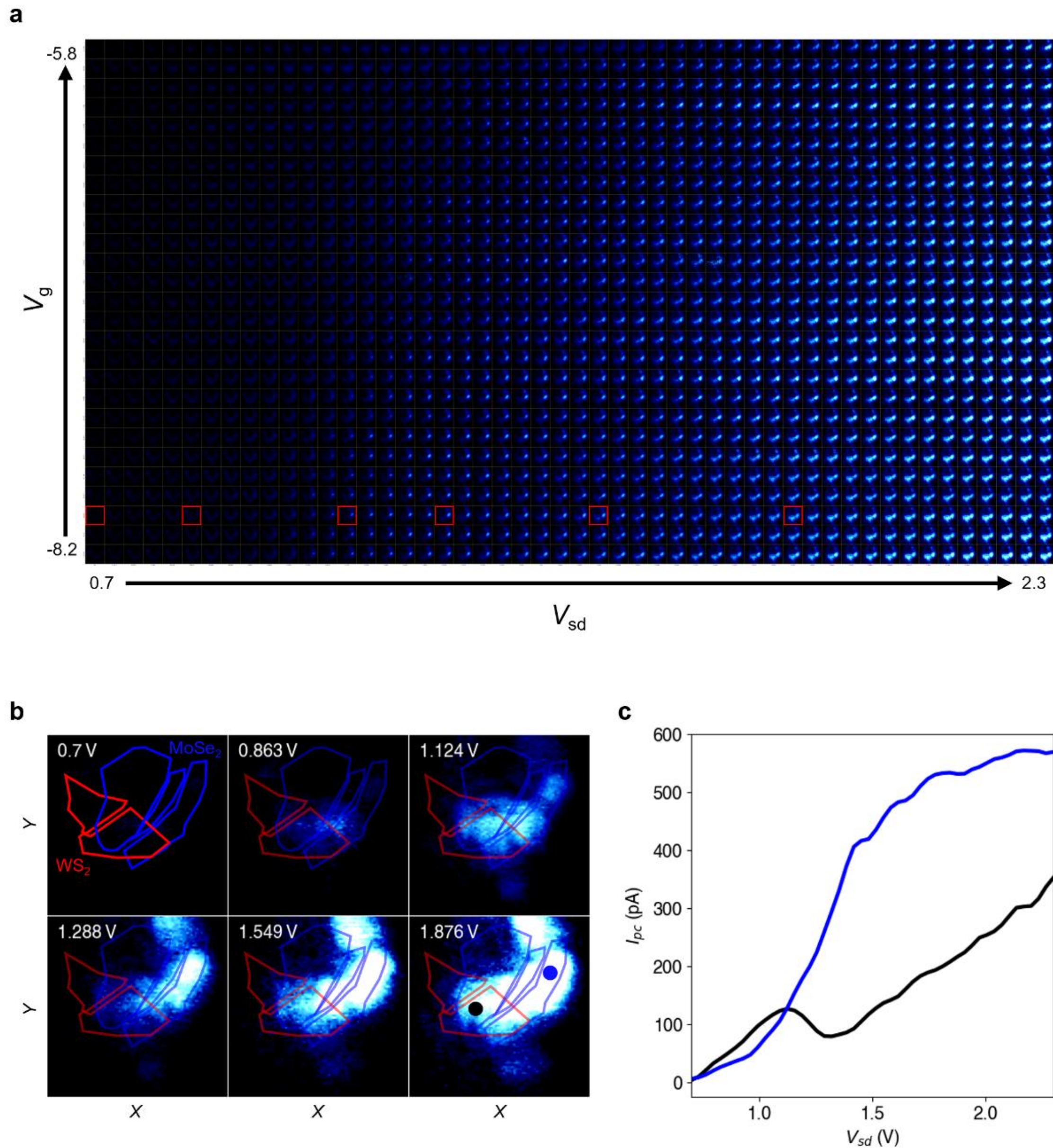

Figure 8.5 | Photocurrent images of device 2 at room temperature with varying Vsd and Vg a, 50x27 hypercube of photocurrent images iterated with changing V_{sd} and V_g. V_{sd} is applied to WS_2 while photocurrent is collected from $MoSe_2$. The laser excitation energy is 1.5eV, nearly resonant with $MoSe_2$ but far below the WS_2 energy gap. **b,** Six selected photocurrent maps, red squares in **a**. $MoSe_2$ and WS_2 flakes are outlined in blue and red respectively. **c,** Extracted I_{pc}-V_{sd} curves for $MoSe_2$ and junction overlap from **a** at the black and blue spots marked in the bottom right panel of **b**. $MoSe_2$ produces monotonically increasing photocurrent. In contrast photocurrent produced at the junction overlap is highly nonlinear and shows a dip as V_{sd} is increased.

The exact I_{pc}-V_{sd} dependance of the overlap and monolayer $MoSe_2$ are extracted by sampling the hypercube at the same spatial point (marked in Figure 8.5b). The resulting curves are shown in figure 8.5c with the overlap in black and $MoSe_2$ in blue. Photocurrent produced from the $MoSe_2$ flake increases monotonically. Photocurrent produced from the overlap initially increases but then peaks and actually decreases with additional voltage. This nonlinear photocurrent is remarkable and entirely contained within the overlap. We next probe the characteristics of the photocurrent suppression to investigate its origin.

8.7 $MoSe_2$/WS_2 junction photocurrent as a function of V_{sd} and V_g

Photocurrent characteristics reveal the anomalous suppression occurs when the chemical potential is in the band gap and may be the result of an electron trap. Figure 8.6 shows photocurrent produced by the heterojunction overlap of device 2 as a function of V_{sd} and V_g. The measurement is performed with V_{sd} applied to WS_2, with a laser excitation of 1.5eV at room temperature. Similar to dark transport, no photocurrent is produced when $V_{sd} < 0.5$V ($V_{sd} < 0$V data is shown in appendix A). At first photocurrent increases with increasing V_{sd}, however a striking photocurrent suppression emerges when positive V_{sd} is tunes between 1.0-1.5V. Figure 8.6b shows I-V_{sd} curves at different V_g voltages clarifying this behavior. As V_g is decreased from 0V to -4.0V the photocurrent suppression deepens.

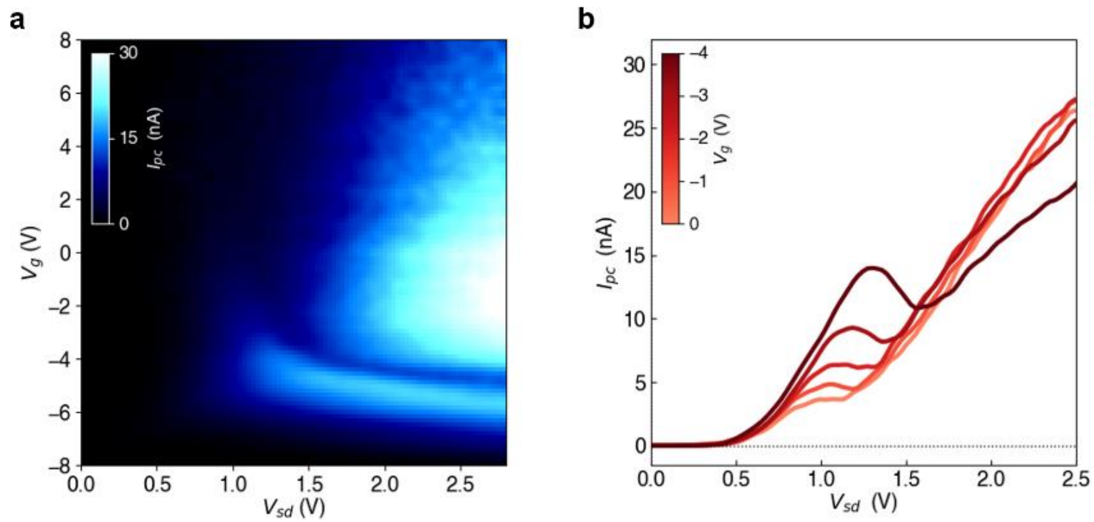

Figure 8.6 | Photocurrent response of $MoSe_2/WS_2$ heterobilayers. a, I_{pc} map as a function of V_{sd} and V_g. **b,** I_{pc}-V_{sd} curves at varying V_g.

Comparing the photocurrent response to dark current over similar voltage values allows us to characterize the anomalous suppression. Figure 8.7 compares dark and photoexcited transport for V_g and V_{sd}. We have previously determined the heterobilayer crosses from charge-neutrality to electon-doped as V_g is increased past -2.0V. I_{pc}-V_g peaks around V_g = -5.0V. A localized photocurrent peak inside the charge neutrality regime is expected for exciton generation. At large V_g the conduction band begins to populate with carriers and bright transitions are Pauli blocked.

The photocurrent suppression with V_{sd} is indicative of charge trapping dynamics. Dark current increases monotonically (Figure 8.7b) as V_{sd} increases, the more electric field we apply through the junction the more current flows though the junction. Photocurrent behaves counter to this, initial generation of electric field through the interface drives increasing current, however, once a critical field is reached additional

field actually *decreases* the charges that exit the heterojunction. Conservation law indicates that either photoexcitation is being quenched or the photoexcited carriers get trapped in the junction until they expire. Relative reflection (Figure 7.2) does show some variation in the absorption however we will see in chapter 9 that the field values do not align. Additionally, reflection data acquired simultaneously with I_{pc} shows no variation.

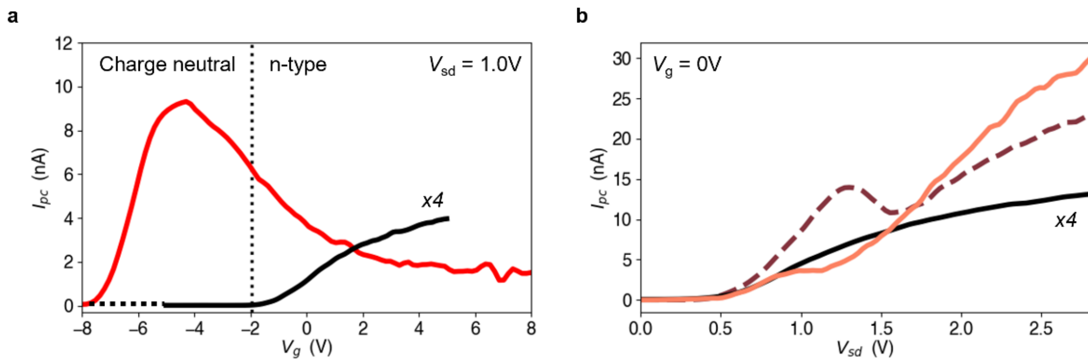

Figure 8.7 | I vs Ipc as a function of Vg and Vsd a, Photocurrent (red) and dark transport (black) as a function of V_g at V_{sd} = 1.0V. Photocurrent peaks around V_g = -5.0V. The previously calculated transition from charge neutrality to n-type doping is marked with the vertical dashed line. The horizontal dashed line extends out the dark transport with data from a separate measurement. **b,** Photocurrent (orange) and dark transport (black) as a function of V_{sd} at V_g = 0V. The dashed dark red curve shows I_{pc}-V_{sd} at V_g = -4.0V. The colors are consistent with figure 8.6b. Dark current monotonically increases with increasing V_{sd} where I_{pc} shows a distinct suppression as V_{sd} is increased. In both panels dark current is multiplied by a factor of 4 to make visible comparison easier.

8.8 I_{pc}-Power: Sublinear power behavior

The laser power dependent photocurrent is used to investigate the origin of the electron trap. Figure 8.8a shows I_{pc}-V_{sd} curves measured with increasing laser power at constant V_g. At low power I_{pc}-V_{sd} is effectively monotonic however as laser power increases the anomalous suppression is introduced and becomes increasingly pronounced.

The photocurrent in this regime exhibits a sublinear power dependence. Figure 8.9b shows I_{pc}-*Power* curves at three different V_{sd}. The degree of curvature is particularly pronounced near the suppression.

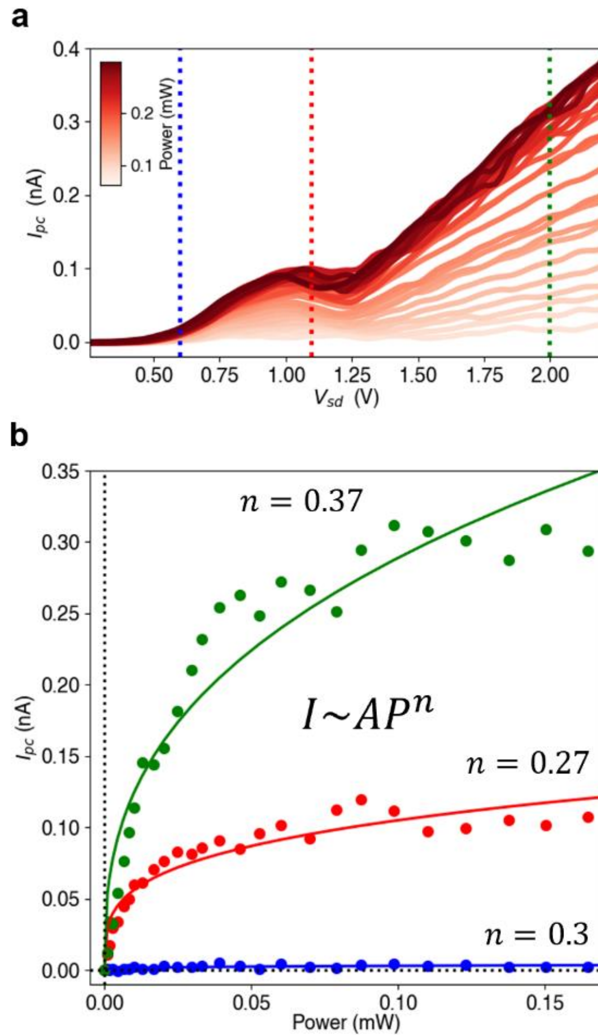

Figure 8.8 | Ipc-Power behavior a, I_{pc}-V_{sd} curves at constant V_g=-6.5V and increasing laser power. The severity of the photocurrent supression deepens as power increases. **b,** I_{pc}-*Power* curves at V_{sd}=0.6V, V_{sd}=1.1V, and V_{sd}=2.0V. These values are marked in **a** with vertical dashed lines.

8.9 Pulsed photoexcitation dynamics

We capture carrier interactions within the junction by implementing a simple pulsed photoexcitation model. As discussed in chapter 5, photocurrent is a direct measure of the number of charge carriers that escape the heterojunction as a result of a laser excitation. The photocurrent

$$I_{pc} = ef\alpha \int_0^\infty N(t)dt \tag{27}$$

depends on the pulse repetition rate f, the extraction rate of carriers α, and the time-dependent population of electron-hole pairs after a pulsed excitation N(t). (27) is valid so long as the repetition period, 1/f, is significantly longer than any transient charge carrier behaviors such that the heterojunction is allowed to return to equilibrium between pulses.

Each laser pulse instantaneously generates a population of N_0 electron-hole pairs. This population decays according to the equation

$$dN/dt = -(\alpha + \beta)N - \gamma N^2 \tag{28}$$

where β is the recombination rate of electron-hole pairs (through radiative or nonradiative processes) and γ is the decay rate due to two-body processes (auger decay, bi-excitonic decay, etc.). The coupling to N and N^2 terms arises as a matter of combinatorics. Figure 8.9 models these three characteristic rates. If N electron hole pairs are generated any single electron can pair and recombine with any of the N holes. In that same N population two electron decay processes have $N \cdot N = N^2$ pairings[iii].

[iii] Bi-exciton decay processes strictly have $N \cdot (N-1)$ pairings but as N_0 for any given laser pulse is very very large this is easily approximated by N^2 as well.

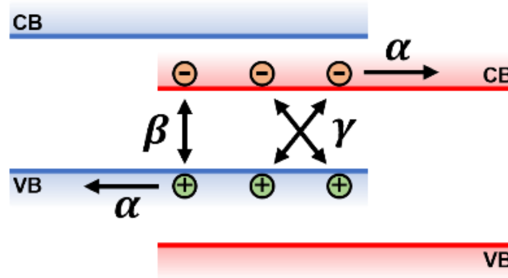

Figure 8.9 | Charge carrier dynamics in a pulsed system

Solving equation (28) gives

$$N(t) = \frac{N_0 e^{-(\alpha+\beta)t}}{1+\frac{\gamma N_0}{\alpha+\beta}\left(1-e^{-(\alpha+\beta)t}\right)} \tag{29}$$

which, when combined with (27) yields an analytic expression for the photocurrent under pulsed excitation:

$$I_{PC} = \frac{ef(\alpha+\beta)}{\gamma} ln\left(\frac{\gamma N_0}{\alpha+\beta} + 1\right) \tag{30}$$

Assuming the initial population scales linearly with laser power, $N_0=c_1P$, we consolidate this to

$$I_{PC} = \frac{\mathrm{B}}{\mathrm{A}} \cdot ln(1 + \mathrm{A}P) \tag{31}$$

where

$$\mathrm{A} = c_1 \frac{\gamma}{\alpha+\beta} \tag{32}$$

$$\mathrm{B} = ef c_2 c_1 \tag{33}$$

A represents the relative rate of multi-particle decay to single body decay scaled to a constant. B contains the laser repetition rate as well an unknown constant, c_2, that consolidates unknown scaling effects such as contact resistance.

8.10 Mapping relative decay rates

Fitting equation (31) to the I_{pc}-*Power* data allows extraction of the relative rate of decay. Figure 8.10a displays the best fit $\gamma/(\alpha+\beta)$ value mapped as a function of V_{sd} and V_g on a logarithmic color scale. The relative decay rate exhibits a striking peak in the same V_{sd} range where the photocurrent is suppressed. Photocurrent and $\gamma/(\alpha+\beta)$ are directly compared in figure 8.10b where we see the photocurrent suppression is concurrent with the peak in relative rate of decay.

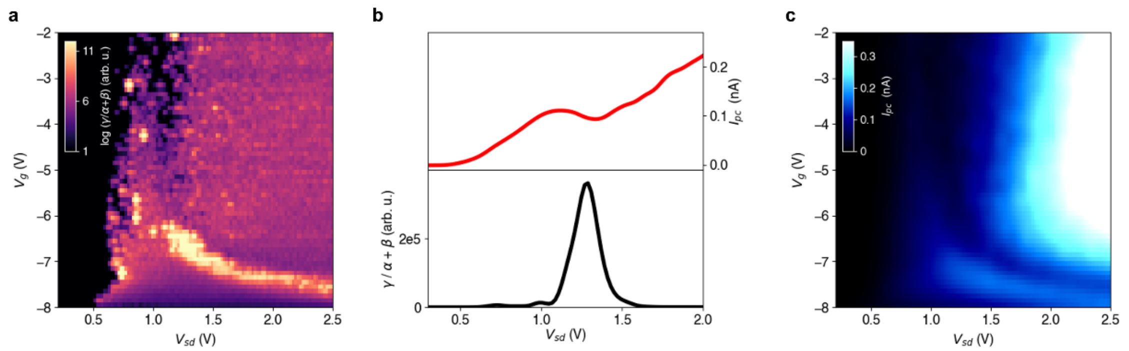

Figure 8.10 | Photocurrent and the relative rate of decay **a,** Map of $\gamma/(\alpha+\beta)$ with respect to V_{sd} and V_g. **b,** I_{pc}-V_{sd} (top) and $\gamma/(\alpha+\beta)$ vs V_{sd} (bottom) **c,** I_{pc} map as a function of V_{sd} and V_g.

The sharp peak in $\gamma/(\alpha+\beta)$ indicates the formation of interlayer excitons. The carrier extraction rate, α, and two-particle decay processes, γ, typically evolve smoothly with V_{sd}. The increase in relative rates is due to a decrease in the electron-hole recombination rate, β. This is consistent with the dominant exciton switching from intra to interlayer. Interlayer excitons have a significantly smaller oscillator strength and thus a small recombination rate. This signifies a direct relationship between the formation of interlayer excitons and the suppression of photocurrent in the heterojunction.

Chapter 9
Envisioning the Invisible

9.1 Building a complete understanding

In the previous two chapters we used PL to map the excitonic energy landscape, dark transport to determine the band alignment, reflectance contrast to map electron-hole excitation, and photocurrent to image relative decay rates. Each of these measurements captures a bit of the optoelectronic behavior of the $MoSe_2/WS_2$ heterobilayer. In this chapter we stitch together these datasets into a single complete whole.

First, I will confirm the intrinsic type-I band alignment in $MoSe_2/WS_2$ and evaluate the excitonic binding energies through PL and dark transport. Stacking all four measurements and aligning them with electric field reveals a depth tunable electron trap that switches on as the heterojunction band alignment is tuned from type-I to type-II. I present redundant measurements from device 4 using gated fields to confirm the effects of V_{sd} control and refine the model. The origin of the trap is revealed to be the formation of interlayer excitons that bind charge carriers inside the heterojunction. Exciton formation, dissociation, and twist dependent recombination can be controlled in situ. Using this model the binding energy of the interlayer exciton is calculated and found to be in agreement with estimations from PL.

9.2 Intrinsic band alignment and excitonic energies

$Mose_2/WS_2$ heterojunctions have been theoretically calculated to have an intrinsic type-II band alignment with nearly degenerate conduction bands. Our experimental results show the intrinsic band alignment is in fact type-I. As discussed in chapter 8.4 dark transport measurements indicate that the $MoSe_2$ conduction band lies at a lower energy than WS_2. From field dependent photoluminescence and previously reported exciton binding energies we can estimate the exact conduction band offset.

We begin by calculating the energy difference between the intralayer exciton, A_{Mo}, and interlayer exciton, IX, in an unbiased junction. The electric field dependence of the interlayer exciton is fit and linearly extrapolated back to zero electric field as shown in figure 9.1a. This indicates the energy of IX at zero field to be ~1.69eV, 90meV higher than the A_{Mo} exciton at 1.60eV.

Exciton binding energies have been previously calculated, based on the effective electron-hole coulomb interactions approximated by the Keldysh potential, in the $MoSe_2/WSe_2$ system. The binding energy of A_{WSe2} was found to be 172.1meV in monolayer[49] and reduced to 152.6meV when stacked in the heterobilayer[50]. In this system the interlayer exciton, $IX_{MoSe2/WSe2}$, was found to have a binding energy of 114meV. The binding energy of A_{MoSe2} has similarly been calculated to be 212.2meV in monolayer[3]. Assuming the $MoSe_2/WS_2$ system exhibits a similar energy reduction due to screening, and a similar ratio of intra to inter layer exciton energies, we estimate the A_{Mo} binding energy to be 212.5 x 90% ≈ 191meV and the *IX* binding energy to be 212.5 x 90% x 75% ≈ 143meV.

Figure 9.1b illustrates the implications of these energies. We know from dark transport that the conduction band of $MoSe_2$ lies below that of WS_2. The band gaps of these materials are 2.0eV and 1.6eV respectively so we know the alignment must be intrinsically type-I. The estimated exciton binding energies of A_{Mo} and IX at 191meV and 143meV are shown with dashed lines. We also know the energy difference between these excitons to be ~90meV from extrapolating the IX emission energy in PL. The offset between the conduction bands is therefore calculated to be 143 + 90 – 191 = 42meV. Notice this indicates the junction transitions from type-I to type-II *before* the interlayer exciton becomes the lowest energy bound state in the system.

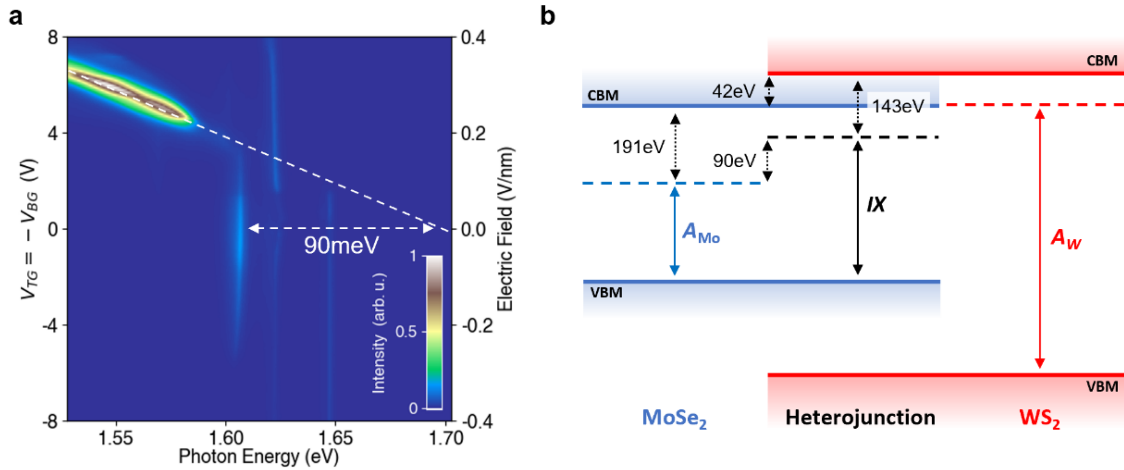

Figure 9.1 | Band alignment and exciton binding energies in $MoSe_2/WS_2$ a, Electric field dependent PL map of $MoSe_2/WS_2$. The IX energy is extrapolated linearly to $V_{bg}=V_{tg}=0V$ where it is found to be ~90meV higher than A_{Mo}. **b,** The energy bands with excitonic band energies in $MoSe_2/WS_2$.

9.3 Tunable band alignment and IX formation in an off twist device

To gain a complete image of the field dependent dynamics in the heterobilayer system we consider together the reflectance contrast, PL, photocurrent, and the relative rate of multi-body to single-body decay interactions. To do so we convert V_{bg}-V_{tg} and V_{sd} to the equivalent out-of-plane electric field (as discussed in sections 3.5 and 3.6). Figure 9.2 shows these four measurements all as a function of electric field. A caveat when directly comparing these measurements is the error in electric field conversion. Error for V_{bg}-V_{tg} is $6x10^{-5}$V/nm while for V_{sd} is 0.012V/nm. This is not enough to fundamentally shift the alignment of the main features discussed below, but fine comparison between the two control methods should be treated with care.

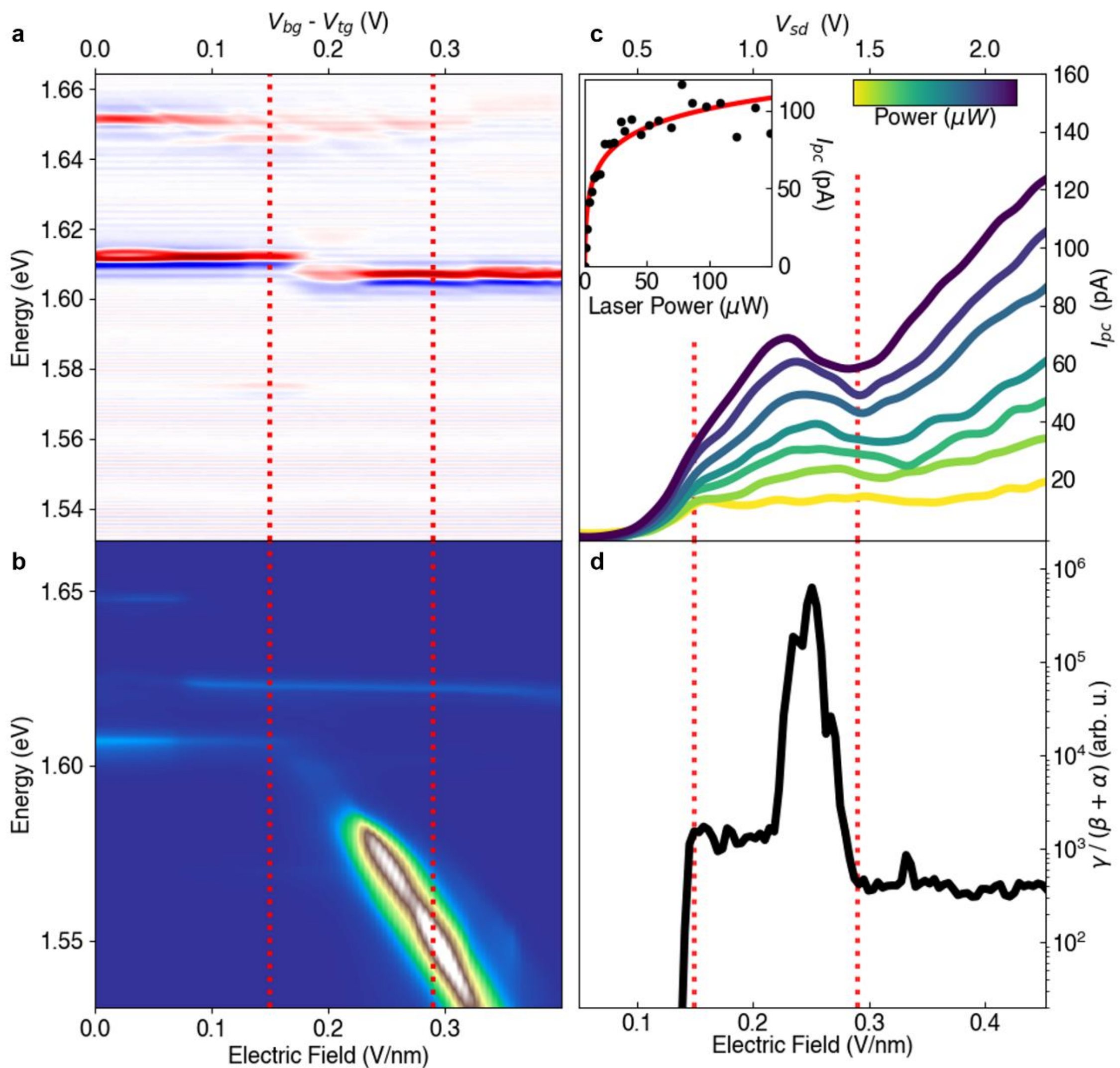

Figure 9.2 | Multi-measurement stitch of $MoSe_2/WS_2$ dynamics in devices 1 and 2 a, Electric field dependent reflectance contrast. **b,** Photoluminescence. **c,** Electric field dependent I_{pc}. **d,** $\gamma/(\alpha+\beta)$. Vertical red dashed lines are at 0.15V/nm and 0.29V/nm.

At low but increasing electric field the primary photoexcitation and photoemission is the formation and radiative recombination of the $MoSe_2$ intralayer exciton, A_{Mo}. In this regime photocurrent turns on exponentially and the relative rate of decay is zero ($(\alpha+\beta)>>\gamma$). At a critical field of 0.16V/nm (vertical black dashed line in

figures 9.2) there is a dramatic shift. As field increases PL emission begins to linearly redshift, I_{pc} ceases to behave exponentially and exhibits a kink, and $\gamma/(\alpha+\beta)$ rises to an appreciable value. Additionally, reflection contrast shows a discontinuity and slight redshift indicating an energetic crossing and state mixing. As electric field is increased past 0.235V/nm (vertical blue dashed line) reflection contrast settles and PL intensity increases dramatically. At this point I_{pc} is suppressed, and $\gamma/(\alpha+\beta)$ exhibits a distinct peak. At fields larger than 0.3V/nm I_{pc} begins to monotonically increase and $\gamma/(\alpha+\beta)$ settles to a static value. PL intensity appears to begin to reduce as well.

These behaviors can be explained by electrical control of the energy landscape driving the formation of interlayer excitons that trap charge carriers at the junction overlap. Figure 9.3 visualizes this model with three regimes: type-I, type-II binding, type-II dissociating. In all three regimes electron-holes pairs originate as photoexcited intralayer excitons in $MoSe_2$. Below the critical field of 0.16V/nm the heterobilayer has a type-I band alignment. A_{Mo} may radiatively recombine, however application of field can drive the electron from the $MoSe_2$ conduction band to WS_2. This dynamic is isometric to that of the pn junction observed in dark transport which is observed by the exponential dependance on V_{sd}.

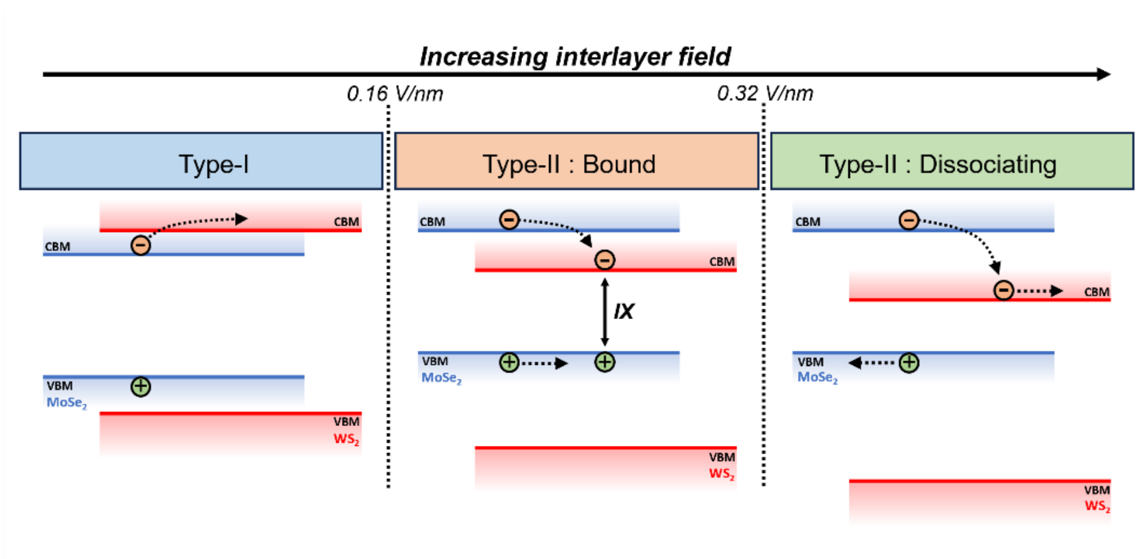

Figure 9.3 | Model for type-I to type-II alignment control and exciton binding vs. dissociation

Once the critical field is surpassed the band alignment is switched from type-I to type-II. With the type-II alignment interlayer excitons begin to form, trapping charge carriers at the interface and suppressing I_{pc}. This trapping and the flat conduction bands turn off the exponential photocurrent behavior. At the immediate alignment transition the energies of IX and A_{Mo} are separated by only ~48meV. This, and the shared position of the exciton hole in $MoSe_2$, causes significant state mixing. As electric field increases IX is shifted to lower energies. Once 0.235V/nm is surpassed the states become energetically separated. The dominance of IX in the system maximizes charge trapping driving the peak suppression in photocurrent. Large enough electric field, $E > 0.3$V/nm, induces dissociation of the interlayer exciton back into free carriers, thus breaking the trap.

9.4 Binding energy and dissociation estimation via I_{pc}

We can estimate the binding energy of the interlayer exciton from I_{pc}. At the critical field IX and A_{Mo} states mix. It is not until the field is increased that I_{pc} is significantly suppressed, indicating IX has fully separated from A_{Mo} and is maximally trapping carriers. If we take the band alignment transition to occur at the kink in I_{pc} and A_{Mo}/IX separation to occur at the start of the γ/(α+β) peak we can calculate the energy difference between the A_{Mo} and IX binding energies to be

$$\Delta U = q\Delta V = e\left(0.23\, {}^{V}\!/_{nm} - 0.149\, {}^{V}\!/_{nm}\right) \cdot 0.65nm = 53meV$$

Using the previously estimated A_{Mo} binding energy of 191meV this yields an IX binding energy of 138meV, which agrees with our theoretical estimate in section 9.2.

We can also attempt to directly estimate the IX binding energy from electric field induced dissociation. We take the critical field value for dissociation to occur at the peak in γ/(α+β). Additional field past this point reduces the relative decay rate. This correlates to a field of 0.26V/nm or an energy of 156meV.

9.5 0 twist V_{bg}-V_{tg} control: exciton-polaron trapping

A key subtlety in the above discussion is that the reflectance contrast and PL measurements were taken from device 1 which has 0/60° twist between $Mose_2$ and WS_2. Dark current and I_{pc} were taken from device 2, which is off twist. Interlayer exciton emission is *not* observed in off twist heterobilayers as IX is not momentum direct in this geometry (the K valleys are not concurrent in momentum space, see appendix A for

emission data from off twist devices). The dark IX excitons cannot radiatively recombine. What happens if we perform similar measurements in a 0/60º twist system?

Figure 9.4 stacks PL, I_{pc}, and relative decay rate all from device 4 and tuned with V_{bg}-V_{tg} rather than V_{sd}. PL emission in this device is not as sharp as in device 1 but the linear stark shifting interlayer exciton is observed. I_{pc} shows the anomalous suppression concurrent with a peak in relative decay rate. The large negative photocurrent between 0 and 0.1V/nm originates from the WS_2 flake and is not associated with the heterojunction, this can be seen in figure 9.8.

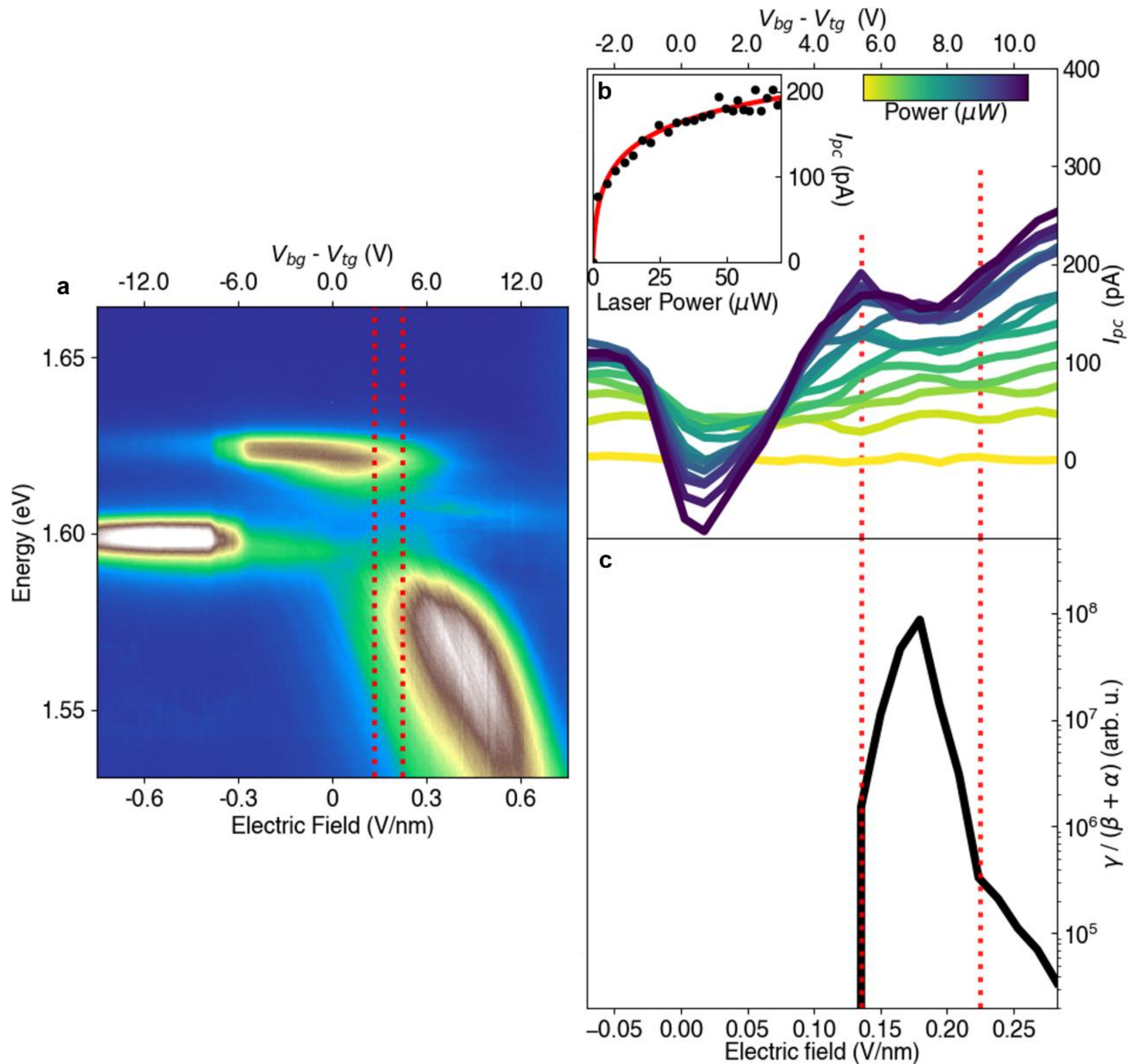

Figure 9.4 | Multi-measurement stitch of $MoSe_2/WS_2$ dynamics in device 4 a, Electric field dependent PL at 4K. **b,** Electric field dependent I_{pc}.**c,** $\gamma/(\alpha+\beta)$ at 50K. Photocurrent is measured from the WS_2 flake. Vertical red dashed lines are at 0.136V/nm and 0.225V/nm.

Photocurrent for this measurement is measured just at the transition of the charge-neutral to electron-doped regime. Figure 9.5 shows doping dependent photoluminescence spectra for device 4 side by side with I_{pc} across similar voltage regimes. I_{pc} for this device is maximized around the n-type transition. Because the PL and I_{pc} measurements are from

the same device we can more meaningfully compare features between them. The peak electric field dependent PL intensity occurs at larger electric field than the $\gamma/(\alpha+\beta)$ peak. We thus propose a modified behavior model for 0/60° twist devices tuned near the A_{Mo}^{+} exciton-polaon regime, described in figure 9.6. Type-I to type-II band alignment is still proposed except now there is additional electron occupation in the conduction band. The bound state now consists of an interlayer exciton-polaron that traps the excess carrier at the junction. This effect is most enhanced while the A_{Mo}^{+} and IX states are mixed. The IX is momentum direct in this device so as the electric field separates the states, IX begins to strongly recombine, freeing the trapped excess charge. This is supported by the critical field values. We proposed that state separation occurring at 0.235V/nm in device 2 drives the primary peak in $\gamma/(\alpha+\beta)$ as the dark exciton is long lived in the off-twist junction. In device 4 $\gamma/(\alpha+\beta)$ turns on at 0.136V/nm and peaks at 0.18V/nm. Assuming an offset in field between the two devices of .024V/nm the relative decay rate peak in device 4 is closer to state separation than to exciton dissociation.

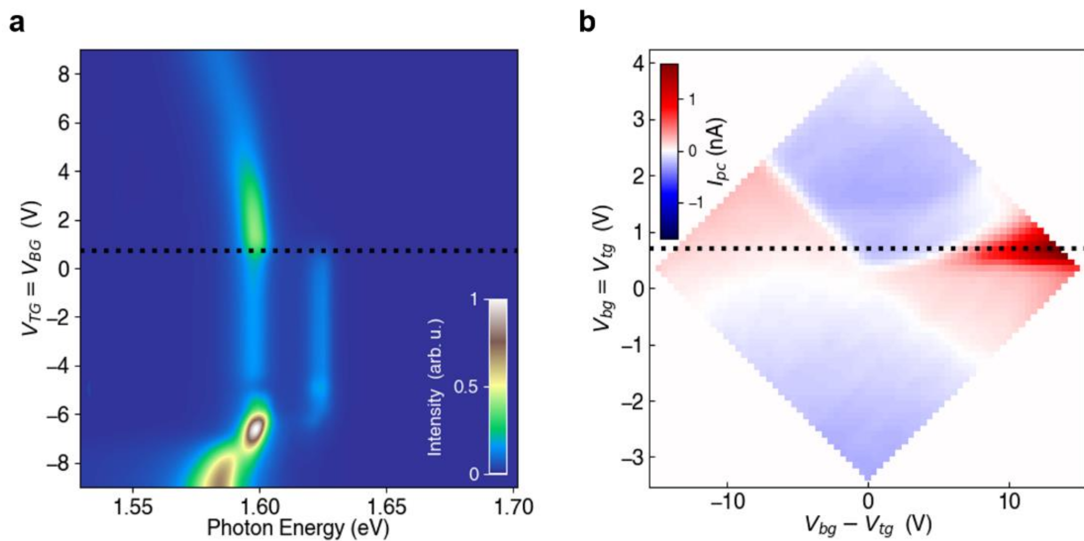

Figure 9.5 | Photoluminescence and photocurrent in device 4 a, Doping dependent PL measured at 4K. **b,** Photocurrent map as a function of V_{bg}-V_{tg} and V_{bg}+V_{tg} at 50K.

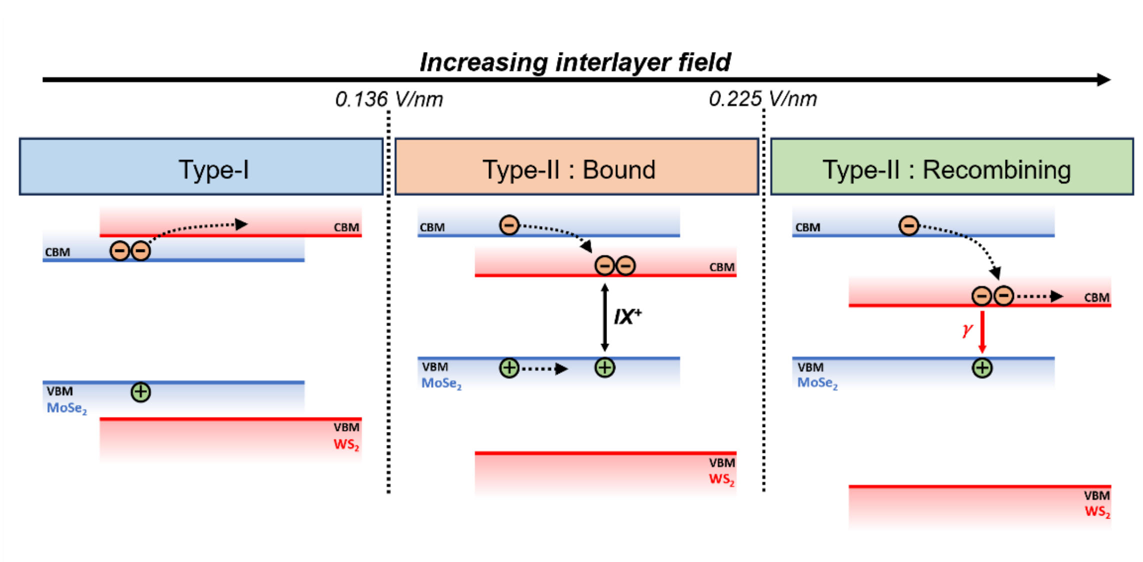

Figure 9.6 | Model for type-I to type-II alignment control and exciton-polaron binding

9.6 Spatial imaging of the electron trap

The most powerful aspect of the above model, informed from diverse but complementary measurements, is that it gives us the requisite knowledge to access a deeper truth from the experimental results. What was before merely a map of nonlinear photocurrent has become a spatial visualization of an exciton modulated electron trap. This behavior cannot be directly observed but now we have gained the power to envision it. Figures 9.7 and 9.8 show the evolution of the spatial photocurrent with increasing electric field in devices 2 and 4. The photocurrent suppression is evident and confined to the heterojunction overlap.

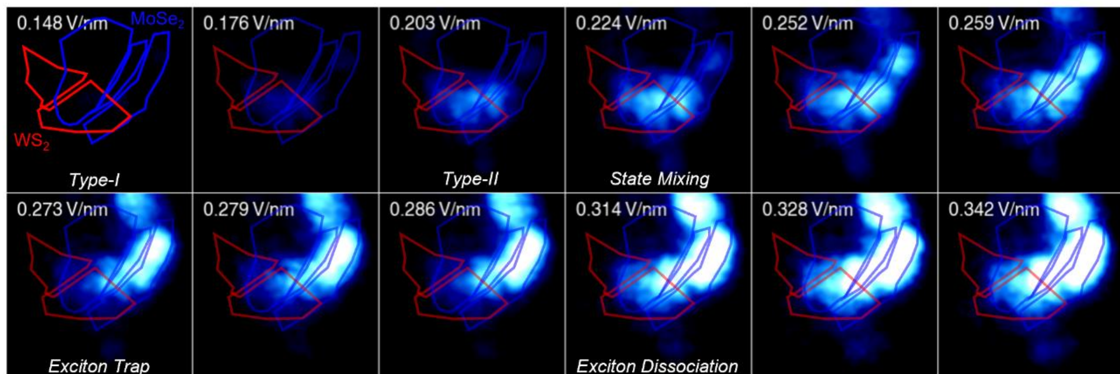

Figure 9.7 | Envisioning a V_{sd} tuned electron trap

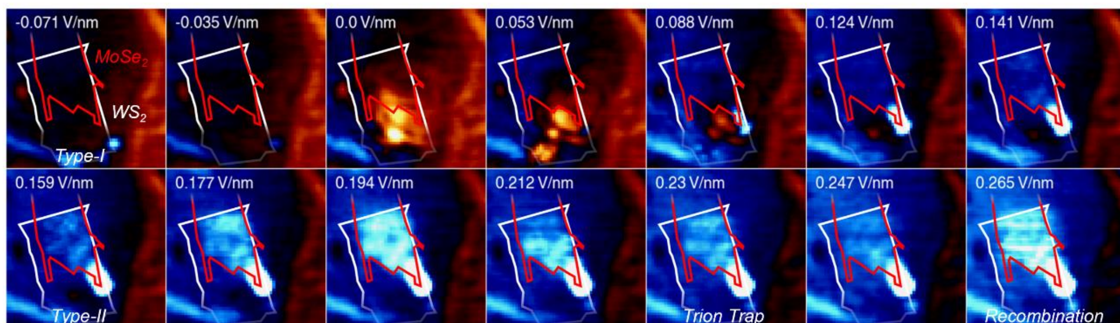

Figure 9.8 | Envisioning a gate tuned electron trap

References

1. Sze, S. M., Li, Y. & Ng, K. K. *Physics of Semiconductor Devices*. (John Wiley & Sons, 2021).

2. Jang, E. & Jang, H. Review: Quantum Dot Light-Emitting Diodes. *Chem. Rev.* **123**, 4663–4692 (2023).

3. Liu, E. *et al.* Exciton-polaron Rydberg states in monolayer MoSe2 and WSe2. *Nat. Commun.* **12**, 6131 (2021).

4. Barbone, M. *et al.* Charge-tuneable biexciton complexes in monolayer WSe2. *Nat. Commun.* **9**, 3721 (2018).

5. Campbell, A. J. *et al.* Exciton-polarons in the presence of strongly correlated electronic states in a MoSe2/WSe2 moiré superlattice. *Npj 2D Mater. Appl.* **6**, 1–8 (2022).

6. Liu, E. *et al.* Excitonic and Valley-Polarization Signatures of Fractional Correlated Electronic Phases in a WSe_2/WS_2 Moiré Superlattice. *Phys. Rev. Lett.* **127**, 037402 (2021).

7. Arp, T. B., Pleskot, D., Aji, V. & Gabor, N. M. Electron–hole liquid in a van der Waals heterostructure photocell at room temperature. *Nat. Photonics* **13**, 245–250 (2019).

8. Wang, P. *et al.* Vertical strain and electric field tunable band alignment in type-II ZnO/MoSSe van der Waals heterostructures. *Phys. Chem. Chem. Phys.* **23**, 1510–1519 (2021).

9. Pham, K. D. *et al.* Vertical strain and electric field tunable electronic properties of type-II band alignment C2N/InSe van der Waals heterostructure. *Chem. Phys. Lett.* **716**, 155–161 (2019).

10. He, J. *et al.* Band Alignment Tailoring of InAs1−xSbx/GaAs Quantum Dots: Control of Type I to Type II Transition. *Nano Lett.* **10**, 3052–3056 (2010).

11. Landmann, M., Rauls, E. & Schmidt, W. G. Understanding band alignments in semiconductor heterostructures: Composition dependence and type-I--type-II transition of natural band offsets in nonpolar zinc-blende $Al_xGa_{1-x}N/Al_yGa_{1-y}N$ composites. *Phys. Rev. B* **95**, 155310 (2017).

12. Yun, J. *et al.* Tunable type-I/type-II transition in g-C3N4/graphyne heterostructure by BN-doping: A promising photocatalyst. *Sol. Energy Mater. Sol. Cells* **210**, 110516 (2020).

13. Zhu, Y., Wan, T., Wen, X., Chu, D. & Jiang, Y. Tunable Type I and II heterojunction of CoOx nanoparticles confined in g-C3N4 nanotubes for photocatalytic hydrogen production. *Appl. Catal. B Environ.* **244**, 814–822 (2019).

14. Meng, Y. *et al.* Electrical switching between exciton dissociation to exciton funneling in MoSe2/WS2 heterostructure. *Nat. Commun.* **11**, 2640 (2020).

15. Nguyen, C. Q. *et al.* Tunable type-II band alignment and electronic structure of $C_3N_4/MoSi_2N_4$ heterostructure: Interlayer coupling and electric field. *Phys. Rev. B* **105**, 045303 (2022).

16. Arp, T. B. *et al.* Quieting a noisy antenna reproduces photosynthetic light-harvesting spectra. *Science* **368**, 1490–1495 (2020).

17. Gabor, N. M., Kistner-Morris, J. & Stewart, B. W. Nature's search for a quiet place. *Phys. Today* **76**, 62 (2023).

18. APS -APS March Meeting 2023 - Event - Planting memes: the shape of information flow in social networks. in *Bulletin of the American Physical Society* (American Physical Society).

19. Ashcroft, N. W. & Mermin, N. D. *Solid State Physics*. (Holt, Rinehart and Winston, 1976).

20. Chaves, A. *et al.* Bandgap engineering of two-dimensional semiconductor materials. *Npj 2D Mater. Appl.* **4**, 1–21 (2020).

21. Sakurai, J. J. & Napolitano, J. *Modern Quantum Mechanics*. (Cambridge University Press, 2017).

22. Mueller, T. & Malic, E. Exciton physics and device application of two-dimensional transition metal dichalcogenide semiconductors. *Npj 2D Mater. Appl.* **2**, 1–12 (2018).

23. Jiang, Y., Chen, S., Zheng, W., Zheng, B. & Pan, A. Interlayer exciton formation, relaxation, and transport in TMD van der Waals heterostructures. *Light Sci. Appl.* **10**, 72 (2021).

24. Hossain, N. *et al.* Recombination mechanisms and band alignment of GaAs1−xBix/GaAs light emitting diodes. *Appl. Phys. Lett.* **100**, 051105 (2012).

25. Sun, Y. *et al.* Band Structure Engineering of Interfacial Semiconductors Based on Atomically Thin Lead Iodide Crystals. *Adv. Mater.* **31**, 1806562 (2019).

26. Lukman, S. *et al.* High oscillator strength interlayer excitons in two-dimensional heterostructures for mid-infrared photodetection. *Nat. Nanotechnol.* **15**, 675–682 (2020).

27. Nguyen, B.-M., Bogdanov, S., Pour, S. A. & Razeghi, M. Minority electron unipolar photodetectors based on type II InAs/GaSb/AlSb superlattices for very long wavelength infrared detection. *Appl. Phys. Lett.* **95**, 183502 (2009).

28. Low, J., Yu, J., Jaroniec, M., Wageh, S. & Al-Ghamdi, A. A. Heterojunction Photocatalysts. *Adv. Mater.* **29**, 1601694 (2017).

29. Yuan, L. *et al.* Broad-spectrum and ultrasensitive photodetectors based on GeSe/SnS2 heterostructures with type-III band alignment. *Appl. Phys. Lett.* **122**, 241106 (2023).

30. Yan, R. *et al.* Esaki Diodes in van der Waals Heterojunctions with Broken-Gap Energy Band Alignment. *Nano Lett.* **15**, 5791–5798 (2015).

31. Zhang, L. *et al.* Twist-angle dependence of moiré excitons in WS2/MoSe2 heterobilayers. *Nat. Commun.* **11**, 5888 (2020).

32. Luryi, S. Quantum capacitance devices. *Appl. Phys. Lett.* **52**, 501–503 (1988).

33. Lee, C.-H. *et al.* Atomically thin p–n junctions with van der Waals heterointerfaces. *Nat. Nanotechnol.* **9**, 676–681 (2014).

34. Schranghamer, T. F., Sharma, M., Singh, R. & Das, S. Review and comparison of layer transfer methods for two-dimensional materials for emerging applications. *Chem. Soc. Rev.* **50**, 11032–11054 (2021).

35. Li, Y., Kuang, G., Jiao, Z., Yao, L. & Duan, R. Recent progress on the mechanical exfoliation of 2D transition metal dichalcogenides. *Mater. Res. Express* **9**, 122001 (2022).

36. Lukose, R. *et al.* Influence of plasma treatment on SiO2/Si and Si3N4/Si substrates for large-scale transfer of graphene. *Sci. Rep.* **11**, 13111 (2021).

37. Marinov, D. *et al.* Reactive plasma cleaning and restoration of transition metal dichalcogenide monolayers. *Npj 2D Mater. Appl.* **5**, 1–10 (2021).

38. Zeng, H. *et al.* Optical signature of symmetry variations and spin-valley coupling in atomically thin tungsten dichalcogenides. *Sci. Rep.* **3**, 1608 (2013).

39. Tonndorf, P. *et al.* Photoluminescence emission and Raman response of monolayer MoS2, MoSe2, and WSe2. *Opt. EXPRESS* **21**, 4908–4916 (2013).

40. Alexeev, E. M. *et al.* Imaging of Interlayer Coupling in van der Waals Heterostructures Using a Bright-Field Optical Microscope. *Nano Lett.* **17**, 5342–5349 (2017).

41. Iwasaki, T. *et al.* Bubble-Free Transfer Technique for High-Quality Graphene/Hexagonal Boron Nitride van der Waals Heterostructures. *ACS Appl. Mater. Interfaces* **12**, 8533–8538 (2020).

42. Tebyetekerwa, M. *et al.* Mechanisms and Applications of Steady-State Photoluminescence Spectroscopy in Two-Dimensional Transition-Metal Dichalcogenides. *ACS Nano* **14**, 14579–14604 (2020).

43. Ma, Q., Krishna Kumar, R., Xu, S.-Y., Koppens, F. H. L. & Song, J. C. W. Photocurrent as a multiphysics diagnostic of quantum materials. *Nat. Rev. Phys.* **5**, 170–184 (2023).

44. Cunningham, P. D., McCreary, K. M. & Jonker, B. T. Auger Recombination in Chemical Vapor Deposition-Grown Monolayer WS2. *J. Phys. Chem. Lett.* **7**, 5242–5246 (2016).

45. Arp, T. B. & Gabor, N. M. Multiple parameter dynamic photoresponse microscopy for data-intensive optoelectronic measurements of van der Waals heterostructures. *Rev. Sci. Instrum.* **90**, 023702 (2019).

46. MacNeill, D. *et al.* Breaking of Valley Degeneracy by Magnetic Field in Monolayer $MoSe_2$. *Phys. Rev. Lett.* **114**, 037401 (2015).

47. Ross, J. S. *et al.* Electrical control of neutral and charged excitons in a monolayer semiconductor. *Nat. Commun.* **4**, 1474 (2013).

48. Tang, Y. *et al.* Tuning layer-hybridized moiré excitons by the quantum-confined Stark effect. *Nat. Nanotechnol.* **16**, 52–57 (2021).

49. Liu, E. *et al.* Magnetophotoluminescence of exciton Rydberg states in monolayer WS_2. *Phys. Rev. B* **99**, 205420 (2019).

50. Liu, E. *et al.* Signatures of moiré trions in WSe2/MoSe2 heterobilayers. *Nature* **594**, 46–50 (2021).

Appendix A
Additional Datasets

A.1 V_{sd}<0 Photocurrent

An astute reader may notice the photocurrent measurements presented in chapter 8 are only performed for positive V_{sd}. When negative V_{sd} is applied to the WS_2 flake, or positive V_{sd} is applied to the $MoSe_2$ flake, the heterobilayer produces near zero photocurrent when in the charge neutrality regime. Figure A1 shows a photocurrent map from device 2 when V_{sd}<0V is applied to WS_2.

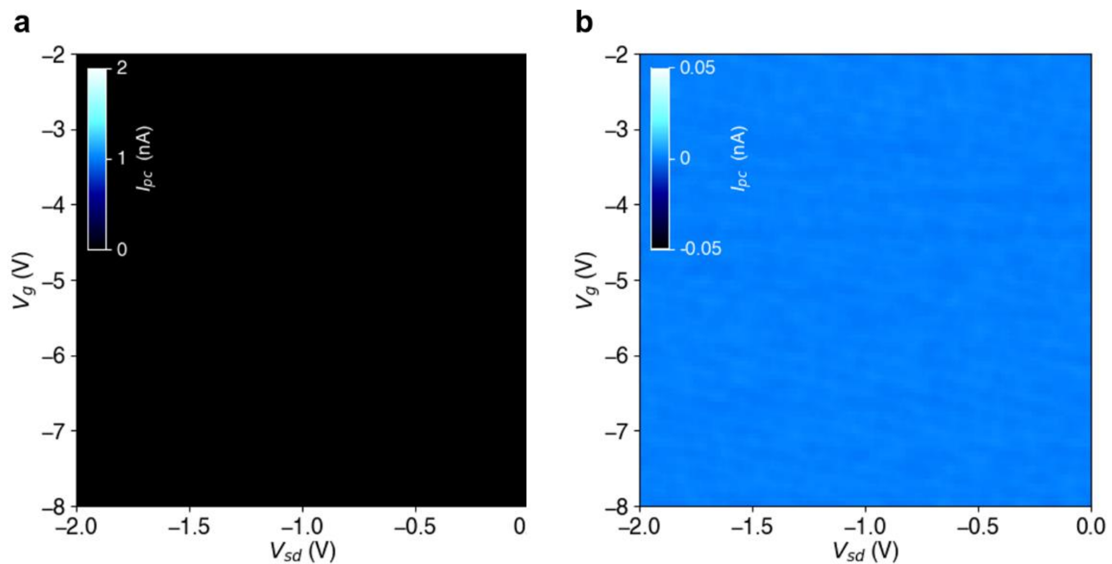

Figure A1 | Reverse bias photocurrent in device 2 a, Photocurrent map with V_{sd} and V_g. V_{sd} is applied to WS_2. **b,** The same photocurrent map as in **a** but the scaling is enhanced until the measurement noise is visible

A.2 $\mathbf{I_{pc}}$*-*$\mathbf{V_{sd}}$ *characteristics in device 4*

Photocurrent mapping as a function of V_{sd} was also performed on a dual graphite gate device. The anomalous photocurrent suppression was observed with similar characteristics to the measured I_{pc} in device 2.

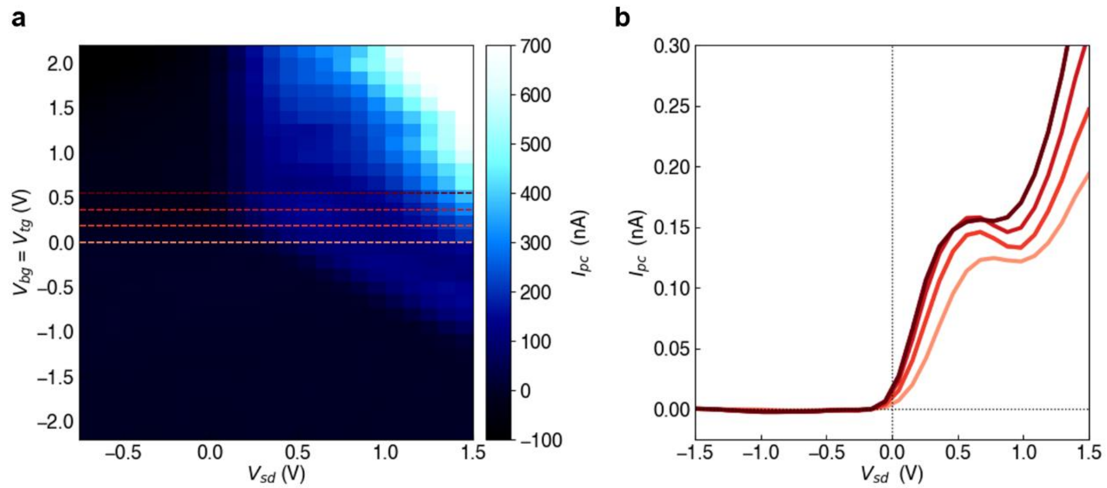

Figure A2 | Photocurrent response of device 4 at room temperature a, Photocurrent map as a function of V_{sd} and V_{bg}=V_{tg}. Equal voltages are applied to the top and bottom gates while interlayer field is driven by V_{sd}. **b,** I_{pc}-V_{sd} curves at V_{bg}=V_{tg} = 0.0V, 1.7V, 3.2V, and 5.0V. There is a distinct photocurrent dip around V_{sd} = 1.0V.

A.3 PL of an off-twist device

The PL measurements presented in the main text were performed on heterobilayers with the MoSe2 and WS2 flakes oritented at 0o or 60o relative to each other. This twist orientation aligns the K valleys of the two materials in momentum space producing a bright interalyer exciton. We also measured PL on an off twist device. The MoSe2 intraleyer exciton emission is observed however at high electric field the linearly stark shifting interlayer exciton emission does not emerge. This is expected as IX in an

off twist heterobilayer is momentum indirect and therefore dark. However, there is a modulation of exciton energies and intensities at certain electric fields. We believe that this is an indirect signature of the band alignment transition, as the band crossover may affect charge transfer dynamics, and so excitonic emissions.

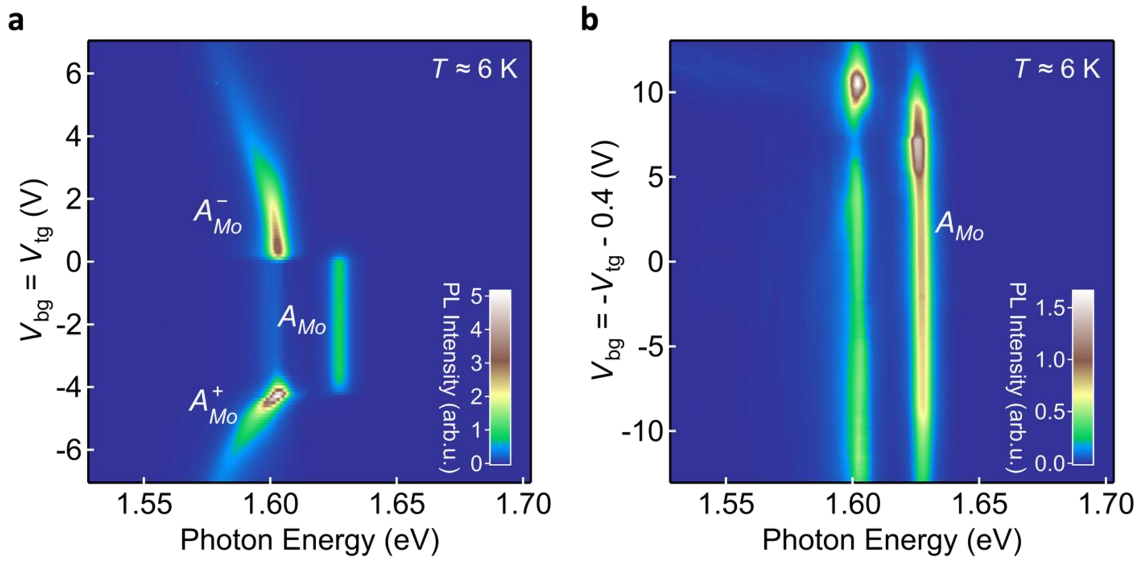

Figure A3 | Doping and electric field dependent photoluminescence response of an off-twist device a, Charge-density-dependent PL map. Equal voltages $V_{bg}=V_{tg}$ are applied to the bottom and top gates. The charge density is proportional to the gate voltages. **b,** The electric-field-dependent PL map. Opposite voltages $V_{bg} = -V_{tg} - 0.4$ are applied to the bottom and top gates to induce an interlayer electric field. All measurements were performed with 532-nm laser excitation (incident power ≈ 3 μW) at sample temperature T ≈ 6 K, the same as the conditions for Device 1 in chapter 7.

A.4 Doping and electric field dependent photoluminescence response of device 3

Figure A4 shows doping and electric field dependent photoluminescence from an additional dual gate device reproducing the primary results presented in chapter 7.

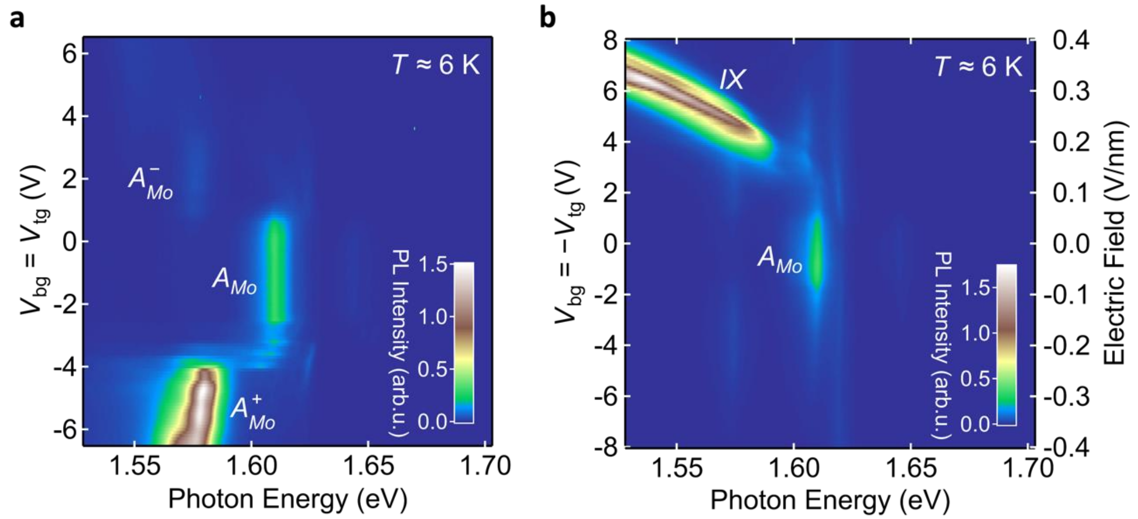

Figure A4 | Doping and electric field dependent photoluminescence map of device 3
a, Charge-density-dependent PL map. Equal voltages $V_{bg} = V_{tg}$ are applied to the bottom and top gates. The charge density is proportional to the gate voltages. The A_{Mo}, A^-_{Mo}, A^+_{Mo} features arise from the intralayer excitons, electron-side and hole-side exciton polarons (or trions) in the $MoSe_2$ layer, respectively. **b,** Electric-field-dependent PL map. Opposite voltages $V_{bg} = -V_{tg}$ (left axis) are applied to the bottom and top gates to induce an interlayer electric field (right axis). An interlayer exciton (IX) feature appears at high electric field. All measurements were performed with 532-nm laser excitation (incident power ≈ 3 μW) at sample temperature $T \approx 6$ K, the same as the conditions for Device 1 in chapter 7.

Appendix B

Electric Field Extraction from the Diode Fit

To extract the out-of-plane electric field generated by applying V_{sd} across an interface, we fit the low voltage exponential I-V_{sd} curve to the diode equation,

$$I(V_{SD}) = I_0(e^{enV_{sd}/k_BT} + 1) \tag{1}$$

If the reverse bias current, I_0, is small we can simplify this to

$$I(V_{sd}) = Ae^{aV_{sd}} \tag{2}$$

where

$$a = \frac{en}{k_BT} \quad , \quad n = \frac{k_BTa}{e} \tag{3}$$

The voltage drop across the interface is given by nV_{sd} and so the of plane field is E = nV_{sd}/d. We take d as the separation between the metal ions of the two monolayers in the heterobilayer. Figure B1e shows the original dark transport measurement from device 2 while figure B1f shows the same data but with the x-axis modified to nV_{sd}. Different V_g produce different n and so the map is continuously contorted in the remapping.

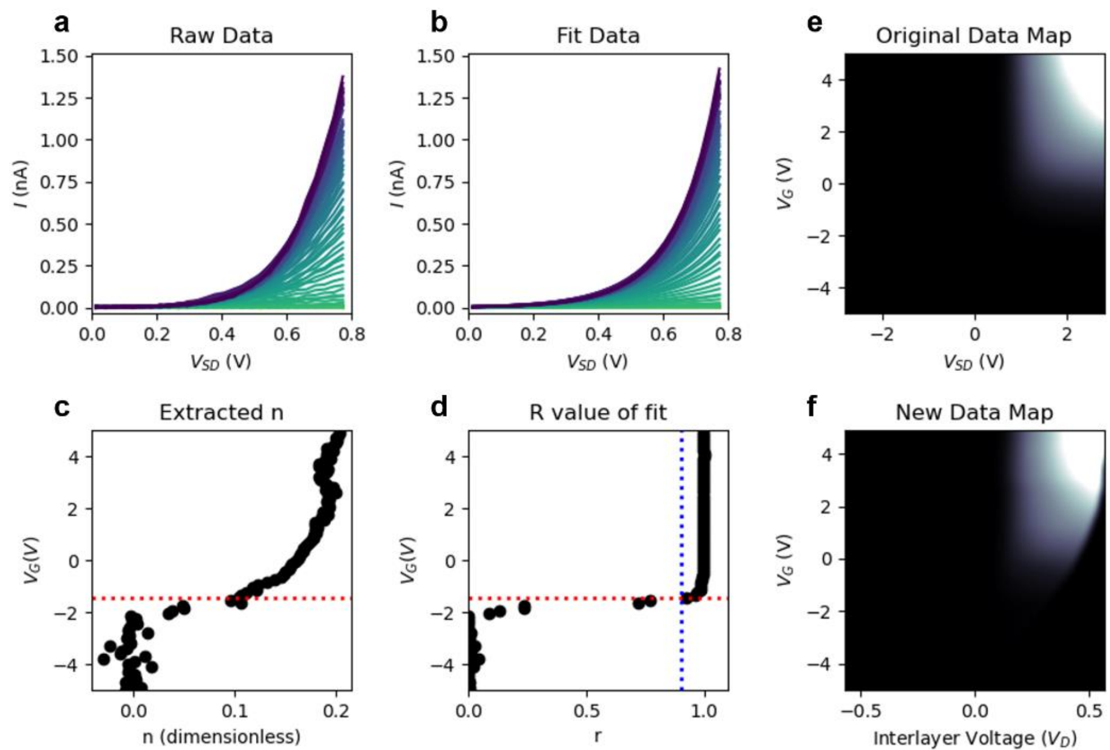

Figure B1 | Interlayer voltage extraction from dark transport in device 2 a, I-V_{sd} curves at different V_g. **b,** Best fit curves of data in panel a. **c,** Extracted ideality factor, n, at different V_g. **d,** R value for different fits. The horizontal red line denotes the cutoff point at which the r value for the fit drops below 0.9 (blue dashed line). **e,** Dark current map as a function of V_{sd} and V_g. **f,** The same dark current map corrected to be a function of the interlayer voltage and V_g. The bottom right section of the map is trimmed because of the axis rescaling.

Appendix C

A Puzzling Perspective

The below characters may seem gibberish, but only for a missing perspective. Application of the mapping described in figure C1 is left as an exercise for the reader.

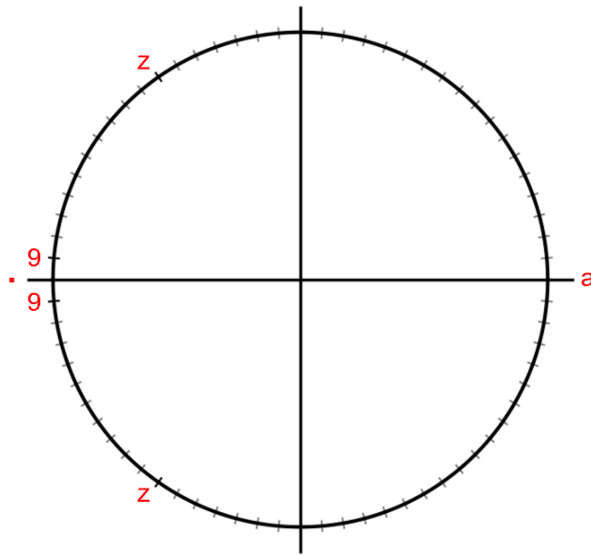

Figure C1 | Unit circle. A circle crossed by vertical and horizontal lines with evenly spaced ticks.

0.985,0.342,0.423,0.866,0.087,1.000,-0.087,-0.174,0.574,1.000,-0.087,0.766,0.342,0.423,0.000,,0.996,-0.174,-0.087,,-0.087,0.819,0.940,,0.259,-0.174,-0.574,-0.574,0.574,0.940,,0.819,1.000,0.000,,0.342,0.423,0.574,-0.500,,0.996,0.940,0.866,-0.174,0.423,-1.000,,0.423,0.342,-0.342,,-0.342,0.940,-0.087,,-0.500,0.342,-0.174,0.087,,-0.342,0.766,-0.087,,1.000,0.423,0.966,,0.259,0.087,0.940,0.259,1.000,0.087,0.940,,0.906,0.342,0.087,,1.000,,-0.342,1.000,0.574,0.643,,0.906,0.342,0.087,,0.906,0.766,0.866,-0.174,0.087,0.940,,0.985,-0.766,,0.766,0.000,,0.819,0.766,0.966,0.966,0.940,0.423,,0.766,0.423,,0.500,1.000,-0.087,0.

940,0.087,0.766,1.000,0.574,0.000,,0.000,0.985,0.766,0.940,0.423,0.985,0.940,,1.000,0.423,0.966,,0.940,0.423,0.866,0.766,0.423,0.940,0.940,0.087,0.766,0.423,0.866,-1.000

0.966,0.342,-0.087,,-0.500,0.342,-0.174,0.087,,0.766,,1.000,0.423,0.966,,0.996,1.000,0.087,,-0.500,0.342,-0.174,0.087,,0.819,,0.906,0.342,0.087,,-0.087,0.819,0.940,0.087,0.940,,0.766,0.000,,0.707,0.342,-0.500,,0.766,0.423,,0.259,0.087,0.940,0.985,0.766,0.000,0.766,0.342,0.423,,1.000,0.423,0.966,,0.643,0.423,0.342,-0.342,0.574,0.940,0.966,0.866,0.940,,0.766,0.423,,-0.174,0.423,0.985,0.940,0.087,-0.087,1.000,0.766,0.423,-0.087,-0.500,-1.000,,0.766,0.423,,-0.087,0.819,0.940,,0.996,-0.174,0.766,0.574,0.966,0.766,0.423,0.866,,-0.342,0.819,0.940,0.087,0.940,,0.819,0.940,-0.087,0.940,0.087,0.342,0.707,-0.174,0.423,0.985,-0.087,0.766,0.342,0.423,0.000,,1.000,0.087,0.940,,0.500,1.000,0.966,0.940,,1.000,0.423,0.966,,0.996,0.087,0.342,0.643,0.940,0.423,,0.000,-0.087,1.000,0.423,0.966,,-0.342,0.819,0.940,0.087,0.940,,0.342,-0.087,0.819,0.940,0.087,0.000,,-0.087,0.087,0.940,1.000,0.966,,-0.259,0.940,0.087,-0.087,0.766,0.985,1.000,0.574,0.574,-0.500,,1.000,0.996,0.342,-0.259,0.940,,1.000,0.423,0.966,,0.000,0.940,0.940,0.643,,-0.087,0.819,0.940,,0.087,0.940,-0.259,0.940,1.000,0.574,0.766,0.423,0.866,,0.985,0.342,0.259,0.259,0.940,0.087,,0.087,0.766,0.423,0.866,-1.000,,-0.174,0.000,0.940,,0.766,-0.087,,-0.087,0.342,,1.000,0.423,0.000,-0.342,0.940,0.087,,-0.087,0.819,0.940,,0.906,0.342,0.574,0.574,0.342,-0.342,0.766,0.423,0.866,-1.000,,1.000,,0.000,-0.087,-0.174,0.966,0.940,0.423,-0.087,,0.766,0.000,,0.985,0.342,0.423,0.906,0.766,0.423,0.940,0.966,,-0.087,0.342,,1.000,0.423,,0.500,0.000,0.940,,0.000,0.766,-0.574,0.940,0.966,,0.996,0.342,-0.423,-1.000,,-0.087,0.819,0.940,0.766,0.087,,0.259,0.342,-0.087,0.940,0.423,-0.087,0.766,1.000,0.574,,0.500,0.342,0.

500,0.940,0.423,-0.087,-0.174,0.500,,0.087,0.940,-0.259,0.940,1.000,0.574,0.000,,-0.087
,0.819,0.940,,0.906,0.766,0.423,1.000,0.574,,0.000,0.259,0.342,-0.087,-1.000,,0.087,1.00
0,0.966,0.766,-0.174,0.000,,1.000,0.423,0.966,,0.966,0.766,1.000,0.500,0.940,-0.087,0.9
40,0.087,,0.819,0.342,0.574,0.966,,-0.087,0.819,0.940,,0.643,0.940,-0.500,-1.000,,0.643,
0.766,0.574,0.342,0.500,0.940,-0.087,0.940,0.087,0.000,,-0.423,-0.500,-1.000,0.423,0.94
0,-0.087,,0.766,0.000,,-0.174,0.423,0.574,0.342,0.985,0.643,0.940,0.966,,0.996,-0.500,,0.
966,0.940,0.985,0.766,0.500,0.940,-0.087,0.940,0.087,0.000,,0.087,0.966,-1.000

0.766,0.423,,-0.087,0.819,0.940,,0.940,-0.259,0.940,0.423,-0.087,,-0.087,0.819,0.940,,0.
087,0.766,0.423,0.866,,0.766,0.000,,0.966,0.940,0.000,-0.087,0.087,0.342,-0.500,0.940,0
.966,,0.342,0.087,,0.766,-0.087,0.000,,0.574,0.342,0.985,1.000,-0.087,0.766,0.342,0.423,
,0.574,0.342,0.000,-0.087,,0.000,0.940,0.940,0.643,0.707,-1.000,0.423,0.940,-0.087,,-0.3
42,0.766,0.574,0.574,,0.985,0.342,0.423,-0.087,1.000,0.766,0.423,,-0.174,0.259,0.966,1.
000,-0.087,0.940,0.966,,0.766,0.423,0.000,-0.087,0.087,-0.174,0.985,-0.087,0.766,0.342,
0.423,0.000,-1.000